Improved distances and ages for stars common to TGAS and RAVE

Paul J. McMillan,[1]* Georges Kordopatis,[2] Andrea Kunder,[3] James Binney,[4]
Jennifer Wojno,[3,5] Tomaž Zwitter,[6] Matthias Steinmetz,[3] Joss Bland-Hawthorn,[7]
Brad K. Gibson,[8] Gerard Gilmore,[9] Eva K. Grebel,[10] Amina Helmi,[11] Ulisse Munari,[12]
Julio F. Navarro,[13] Quentin A. Parker,[14,15] George Seabroke,[16] Fred Watson[17] and
Rosemary F. G. Wyse[5]

[1]*Lund Observatory, Department of Astronomy and Theoretical Physics, Lund University, Box 43, SE-22100 Lund, Sweden*
[2]*Université Côte d'Azur, Observatoire de la Côte d'Azur, CNRS, Laboratoire Lagrange, Parc Valrose, F-06108 Nice, France*
[3]*Leibniz-Institut für Astrophysik Potsdam, An der Sternwarte 16, D-14482 Potsdam, Germany*
[4]*Rudolf Peierls Centre for Theoretical Physics, Keble Road, Oxford OX1 3NP, UK*
[5]*Department of Physics and Astronomy, Johns Hopkins University, 3400 N. Charles St, Baltimore, MD 21218, USA*
[6]*Faculty of Mathematics and Physics, University of Ljubljana, Jadranska 19, 1000 Ljubljana, Slovenia*
[7]*Sydney Institute for Astronomy, School of Physics A28, University of Sydney, NSW 2006, Australia*
[8]*E.A. Milne Centre for Astrophysics, University of Hull, Hull HU6 7RX, UK*
[9]*Institute of Astronomy, University of Cambridge, Madingley Road, Cambridge CB3 0HA, UK*
[10]*Astronomisches Rechen-Institut, Zentrum für Astronomie der Universität Heidelberg, Mönchhofstr. 12–14, D-69120 Heidelberg, Germany*
[11]*Kapteyn Astronomical Institute, University of Groningen, PO Box 800, NL-9700 AV Groningen, the Netherlands*
[12]*INAF Astronomical Observatory of Padova, I-36012 Asiago (VI), Italy*
[13]*Senior CIfAR Fellow, Department of Physics and Astronomy, University of Victoria, Victoria BC V8P 5C2, Canada*
[14]*Department of Physics, The University of Hong Kong, Hong Kong SAR, China*
[15]*The University of Hong Kong, Laboratory for Space Research, Hong Kong SAR, China*
[16]*Mullard Space Science Laboratory, University College London, Holmbury St. Mary, Dorking, Surrey RH5 6NT, UK*
[17]*Australian Astronomical Observatory, PO Box 915, North Ryde, NSW 1670, Australia*

ABSTRACT

We combine parallaxes from the first *Gaia* data release with the spectrophotometric distance estimation framework for stars in the fifth RAVE survey data release. The combined distance estimates are more accurate than either determination in isolation – uncertainties are on average two times smaller than for RAVE-only distances (three times smaller for dwarfs), and 1.4 times smaller than TGAS parallax uncertainties (two times smaller for giants). We are also able to compare the estimates from spectrophotometry to those from *Gaia*, and use this to assess the reliability of both catalogues and improve our distance estimates. We find that the distances to the lowest log *g* stars are, on average, overestimated and caution that they may not be reliable. We also find that it is likely that the *Gaia* random uncertainties are smaller than the reported values. As a by-product we derive ages for the RAVE stars, many with relative uncertainties less than 20 per cent. These results for 219 566 RAVE sources have been made publicly available, and we encourage their use for studies that combine the radial velocities provided by RAVE with the proper motions provided by *Gaia*. A sample that we believe to be reliable can be found by taking only the stars with the flag notification 'flag_any=0'.

Key words: methods: statistical – Galaxy: fundamental parameters – Galaxy: kinematics and dynamics – Galaxy: structure.

1 INTRODUCTION

ESA's *Gaia* mission (Gaia Collaboration 2016a) is an enormous project that is revolutionizing Milky Way astronomy. *Gaia* will provide a wide range of data about the stars of the Milky Way, including photometry and spectroscopy. However it is the astrometry – and in particular the parallaxes – from *Gaia* that are the cause of the most excitement. It is very difficult to determine the distances to stars, and not knowing the distance to a star means that one knows neither where it is nor how fast it is moving, even if the proper motion of the star is known.

*E-mail: paul@astro.lu.se

The RAVE survey (Radial Velocity Experiment; Steinmetz et al. 2006) is a spectroscopic survey that took spectra for ~500 000 stars. From these one could determine for each star its line-of-sight velocity and the structural parameters, such as its effective temperature (T_{eff}), surface gravity (log g), and metallicity ([M/H]). These can be used to derive the distances to stars, and since RAVE's fourth data release (Kordopatis et al. 2013) these have been provided by the Bayesian method that was introduced by Burnett & Binney (2010), and extended by Binney et al. (2014). Bayesian methods had previously been used for distance estimation in astrophysics for small numbers of stars of specific classes (Barnes et al. 2003; Thorstensen 2003), and the Burnett & Binney method is similar to an approach that had previously been used to determine the ages of stars (Pont & Eyer 2004; Jørgensen & Lindegren 2005). Closely related approaches have since been used by numerous studies (e.g. Serenelli et al. 2013; Schönrich & Bergemann 2014; Santiago et al. 2016; Wang et al. 2016; Mints & Hekker 2017; Queiroz et al. 2017; Schneider et al. 2017). The method produces a probability density function (pdf) for the distance, and these pdfs were tested by, amongst other things, comparison of some of the corresponding parallax estimates to the parallaxes found by *Gaia*'s predecessor *Hipparcos* (Perryman et al. 1997; van Leeuwen 2007). RAVE's most recent data release was the fifth in the series (henceforth DR5), and included distance estimates found using this method (Kunder et al. 2017). The RAVE sample appears to be kinematically and chemically unbiased (Wojno et al. 2017).

Gaia's first data release (*Gaia* DR1; Gaia Collaboration 2016b; Lindegren et al. 2016) includes parallaxes and proper motions for ~ 2000 000 sources. These were available earlier than full astrometry for the other ~1 billion sources observed by *Gaia*, because the sources were observed more than 20 yr earlier by the *Hipparcos* mission, and their positions at that epoch (and proper motions) appear in either the *Hipparcos* catalogue or the, less precise, Tycho-2 catalogue (Høg et al. 2000), which used data from the *Hipparcos* satellite's star mapper. This means that the proper motions of the stars can be derived using this very long time baseline, which breaks degeneracies between proper motion and parallax that made the determination of these parameters for the other sources impossible. The resulting catalogue is known as the Tycho-*Gaia* Astrometric solution (TGAS; Michalik, Lindegren & Hobbs 2015).

Since RAVE and TGAS use fundamentally different methods for deriving the distances to stars, it is inevitable that these have different precisions for different types of stars. The Burnett & Binney (2010) method relies, fundamentally, on comparing the observed magnitude to the expected luminosity. The uncertainty in distance modulus, which is roughly equivalent to a relative distance uncertainty, is therefore approximately independent of the distance to the star. The parallax uncertainty from TGAS, on the other hand, is independent of the parallax value, so the relative precision declines with distance – large distances correspond to small parallaxes, and therefore large relative uncertainties.

In Fig. 1 we show the quoted parallax uncertainty from both TGAS and DR5 for the sources common to both catalogues. In the case of TGAS we use the quoted statistical uncertainties (see Section 6 for further discussion). We also divide this into the uncertainty for giant stars (DR5 log g < 3.5) and dwarfs (DR5 log g ≥ 3.5). We see that for TGAS this distinction is immaterial, while it makes an enormous difference for DR5. The DR5 parallax estimates tend to be less precise than the TGAS ones for dwarfs (which tend to be nearby because the survey is magnitude limited), but as precise, or more, for the more luminous giants, especially the more distant ones.
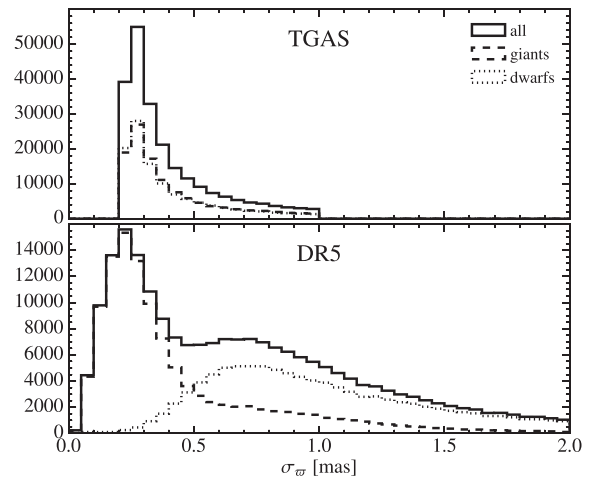

Figure 1. Histograms of the quoted random parallax uncertainties (σ_ϖ) from TGAS and those from RAVE DR5 for stars common to the two catalogues. We show histograms of the uncertainties for all stars (solid), and separately for giants (log g_{DR5} < 3.5) and dwarfs (log g_{DR5} ≥ 3.5). The y-axis gives the number of stars per bin, and there are 40 bins in total in both cases. The cut-off at 1 mas for the TGAS parallaxes is due to a filter applied by the *Gaia* consortium to their DR1. For RAVE sources we make the standard cuts to the catalogue described in Kunder et al. (2017). TGAS parallaxes are more precise than RAVE's for dwarfs, but not necessarily for giants.

It is worth noting that TGAS provides only parallax measurements, not *distance* estimates and, as discussed by numerous authors at various points over the last century, the relationship between one and the other is non-trivial when one takes the uncertainties into account (e.g. Strömberg 1927; Lutz & Kelker 1973; Luri & Arenou 1997; Bailer-Jones 2015). Astraatmadja & Bailer-Jones (2016) looked at how the distances derived from TGAS parallaxes depend on the prior probability distribution used for the density of stars, but did not use any information about a star other than its parallax.

For this reason, and because TGAS parallaxes have large relative errors for distant stars, when studying the dynamics of the Milky Way using stars common to RAVE and TGAS, it has been seen as advantageous to use distances from DR5 rather than those from TGAS parallaxes (e.g. Hunt, Bovy & Carlberg 2016; Helmi et al. 2017). It is therefore important to improve these distance estimates and to check whether there are any systematic errors associated with the DR5 distance estimates.

Kunder et al. (2017) discuss the new efforts in RAVE DR5 to reconsider the parameters of the observed stars. They provided new T_{eff} values derived from the Infrared Flux Method (IRFM; Blackwell, Shallis & Selby 1979) using an updated version of the implementation described by Casagrande et al. (2010). Also provided in a separate data-table were new values of log g following a recalibration for red giants from the Valentini et al. (2017) study of 72 stars with log g values derived from asteroseismology of stars by the K2 mission (Howell et al. 2014). These were not used to derive distances in the main DR5 catalogue, and we now explore how using these new data products can improve our distance estimates.

In this study, we compare parallax estimates from TGAS and RAVE to learn about the flaws in both catalogues. We then include the TGAS parallaxes in the RAVE distance estimation, to derive more precise distance estimates than are possible with either set of data in isolation.

It is also possible to derive ages for stars from the same efforts, indeed the use of Bayesian methods to derive distances was preceded by studies using them to determine ages (Pont & Eyer 2004; Jørgensen & Lindegren 2005). RAVE DR4 included the age estimates derived alongside the distances, but these were recognized as only being indicative (Kordopatis et al. 2013). In this study we show the substantial improvement that is possible using TGAS parallaxes and a more relaxed prior.

In Section 2 we describe the method used to derive distances. In Section 3 we compare results from DR5 to those from TGAS, which motivates us to look at improving our parallax estimates using other RAVE data products in Section 4. In Section 5 we explore the effect of varying our prior. In Section 6 we look at what we can learn about TGAS by comparison with these new parallax estimates. Finally, Sections 7, 8, and 9 demonstrate the improvements made possible by using the TGAS parallaxes as input to the Bayesian scheme.

2 BAYESIAN ESTIMATION

Since RAVE DR4, distances to the stars in the RAVE survey have been determined using the Bayesian method developed by Burnett & Binney (2010). This takes as its input the stellar parameters $T_{\rm eff}$, $\log g$, and [M/H] determined from the RAVE spectra, and J, H, and K_s magnitudes from 2MASS (Skrutskie et al. 2006). This method was extended by Binney et al. (2014) to include dust extinction in the modelling, and introduce an improvement in the description of the distance to the stars by providing multi-Gaussian fits to the full pdf in distance modulus.[1]

In this paper we extend this method, principally by including the parallaxes found by TGAS as input, but also by adding AllWISE $W1$ and $W2$ mid-infrared photometry (Cutri & et al. 2013). We will explore improvements made possible by using IRFM $T_{\rm eff}$ values given in RAVE DR5, rather than $T_{\rm eff}$ derived from the spectra. We expect that the IRFM values can be more precise than those from the RAVE spectra, which only span a narrow range in wavelength (8410–8795 Å).

Because the original intention of this pipeline was to estimate distances, we often refer to it as the 'distance pipeline'. In practice we are now often as interested in its other outputs as we are in the distance estimates. The pipeline applies the simple Bayesian statement

$$P(\text{model}|\text{data}) = \frac{P(\text{data}|\text{model})P(\text{model})}{P(\text{data})}, \qquad (1)$$

where in our case 'data' refer to the inputs described above (and shown in Table 1) for a single star, and 'model' comprises a star of specified initial mass $\mathcal{M}$, age τ, metallicity [M/H], and location relative to the Sun (where Galactic coordinates l and b are treated as known and distance s is unknown), observed through a specified line-of-sight extinction, which we parametrize by extinction in the V-band, A_V. The likelihood $P(\text{data}|\text{model})$ is determined assuming uncorrelated Gaussian uncertainties on all inputs, and using isochrones to find the values of the stellar parameters and absolute magnitudes of the model star. The isochrones that we use are from the PARSEC v1.1 set (Bressan et al. 2012), and the metallicities of the isochrones used are given in Table 2. $P(\text{model})$ is our prior which we discuss below, and $P(\text{data})$ is a normalization constant

[1]While the distance estimates always use 2MASS (and, in this study, All-WISE) photometry, we will refer to them as 'RAVE-only' at various points in this paper, to distinguish them from those found using TGAS parallaxes as input too.

Table 1. Data used to derive the distances to our stars, and their source.

Data	Symbol	Notes
Effective temperature	$T_{\rm eff}$	RAVE DR5 – either from spectrum (DR5) or IRFM
Surface gravity	$\log g$	RAVE DR5
Metallicity	[M/H]	RAVE DR5
J-band magnitude	J	2MASS
H-band magnitude	H	2MASS
K_s-band magnitude	K_s	2MASS
W_1-band magnitude	W_1	AllWISE – not used for DR5 distances
W_2-band magnitude	W_2	AllWISE – not used for DR5 distances
Parallax	ϖ TGAS	*Gaia* DR1 – not used for DR5 distances or in comparisons

Table 2. Metallicities of isochrones used, taking $Z_\odot = 0.0152$ and applying scaled solar composition, with $Y = 0.2485 + 1.78Z$. Note that the minimum metallicity is [M/H] $= -2.2$, significantly lower than for the Binney et al. (2014) distance estimates where the minimum metallicity used was -0.9, which caused a distance underestimation for the more metal-poor stars (Anguiano et al. 2015).

Z	Y	[M/H]
0.00010	0.249	−2.207
0.00020	0.249	−1.906
0.00040	0.249	−1.604
0.00071	0.250	−1.355
0.00112	0.250	−1.156
0.00200	0.252	−0.903
0.00320	0.254	−0.697
0.00400	0.256	−0.598
0.00562	0.259	−0.448
0.00800	0.263	−0.291
0.01000	0.266	−0.191
0.01120	0.268	−0.139
0.01300	0.272	−0.072
0.01600	0.277	0.024
0.02000	0.284	0.127
0.02500	0.293	0.233
0.03550	0.312	0.404
0.04000	0.320	0.465
0.04470	0.328	0.522
0.05000	0.338	0.581
0.06000	0.355	0.680

which we can ignore. The assumption of uncorrelated Gaussian errors on the stellar parameters is one which is imperfect (see e.g. Schönrich & Bergemann 2014; Schneider et al. 2017), but it is the best approximation that we have available for RAVE.

Putting this in a more mathematical form and defining the notation for a single Gaussian distribution

$$G(x, \mu, \sigma) = \frac{1}{\sqrt{2\pi\sigma^2}} \exp\left(\frac{(x-\mu)^2}{2\sigma^2}\right), \qquad (2)$$

we have

$$P(\mathcal{M}, \tau, [\text{M/H}], s, A_V | \text{data}) \propto P(\mathcal{M}, \tau, [\text{M/H}], s, A_V | l, b)$$
$$\times \prod_i G(O_i^T(\mathcal{M}, \tau, [\text{M/H}], s, A_V), O_i, \sigma_i), \qquad (3)$$

where the prior $P(\mathcal{M}, \tau, [\text{M/H}], s, A_V | l, b)$ is described in Section 2.1, and the inputs O_i, σ_i are those given in Table 1 (the cases

where any of these inputs are unavailable or not used can be treated as the case where $\sigma_i \to \infty$). The theoretical values of these quantities – $O_i^T(\mathcal{M}, \tau, [M/H], s, A_V)$ – are found using the isochrones and the relations between extinctions in different bands given in Section 2.1.

Once we have calculated the pdfs $P(\text{model}|\text{data})$ for the stars we can characterize them however we wish. In practice, we characterize them by the expectation values and standard deviation (i.e. estimates and their uncertainties) for all parameters, found by marginalizing over all other parameters.

For distance we find several characterizations of the pdf: expectation values and standard deviation for the distance itself (s), for distance modulus (μ), and for parallax ϖ. The characterization in terms of parallax is vital for comparison with TGAS parallaxes.

In addition we provide multi-Gaussian fits to the pdfs in distance modulus because a number of the pdfs are multimodal, typically because it is unclear from the data whether a star is a main-sequence star or a (sub-)giant. Therefore, a single expectation value and standard deviation is a poor description of the pdf. The multi-Gaussian fits to the pdfs in μ provide a compact representation of the pdf, and following Binney et al. (2014) we write them as

$$P(\mu) = \sum_{k=1}^{N_{\text{Gau}}} f_k G(\mu, \widehat{\mu_k}, \sigma_k), \qquad (4)$$

where the number of components N_{Gau}, the means $\widehat{\mu_k}$, weights f_k, and dispersions σ_k are determined by the pipeline.

To determine whether a distance pdf is well represented by a given multi-Gaussian representation in μ we take bins in distance modulus of width $w_i = 0.2$ mag, which contain a fraction p_i of the total probability taken from the computed pdf and a fraction P_i from the Gaussian representation, and compute the goodness-of-fit statistic

$$F = \sum_i \left(\frac{p_i}{w_i} - \frac{P_i}{w_i}\right)^2 \tilde{\sigma} w_i, \qquad (5)$$

where the weighted dispersion

$$\tilde{\sigma}^2 \equiv \sum_{k=1,N_{\text{Gau}}} f_k \sigma_k^2 \qquad (6)$$

is a measure of the overall width of the pdf. Our strategy is to represent the pdf with as few Gaussian components as possible, but if the value of F is greater than a threshold value ($F_t = 0.04$), or the standard deviation associated with the model differs by more than 20 per cent from that of the complete pdf, then we conclude that the representation is not adequate, and add another Gaussian component to the representation (to a maximum of three components, which we have found is almost always enough). We fit the multi-Gaussian representation to the histogram using the Levenberg–Marquandt algorithm (e.g. Press, Flannery & Teukolsky 1986), which we apply multiple times with different starting points estimated from the modes of the distribution. In this way we can take the best result and therefore avoid getting caught in local minima. The relatively broad bins mean that we only use more than one Gaussian component if the pdf is significantly multimodal, though this comes at the cost of reducing the accuracy of the fit when a peak is narrow.

These multi-Gaussian fits were particularly important in previous RAVE data releases. In DR5 we found that a single Gaussian component proved adequate for only 45 per cent of the stars, while around 51 per cent are fitted with two Gaussians, and only 4 per cent require a third component. In Section 7 we show that the addition of TGAS parallaxes substantially reduces the number of stars for which more than one Gaussian is required.

The value of F is provided in the data base as FitQuality_Gauss, and we also include a flag (denoted Fit_Flag_Gauss) which is non-zero if the standard deviation of the final fitted model differs by more than 20 per cent from that of the computed pdf. Typically, the problems flagged are rather minor (as shown in fig. 3 of Binney et al. 2014).

The uncertainties of the RAVE stellar parameters are assumed to be the quadratic sum of the quoted internal uncertainties and the external uncertainties (table 4 of DR5). The external uncertainties are those calculated from stars with an SNR>40, except in the case of the IRFM temperatures for which a single uncertainty serves for stars of every SNR since the IRFM temperatures are not extracted from the spectra. We discard all observations with a signal-to-noise ratio less than 10, or where the RAVE spectral pipeline returns a quality flag (AlgoConv) of '1', because the quoted parameters for these observations are regarded as unreliable.

For the 2MASS and AllWISE photometry we use the quoted uncertainties. We discard the AllWISE magnitudes if they are brighter than the expected saturation limit in each band, which we take to be $W_{1,\text{sat}} = 8.1$ mag, and $W_{2,\text{sat}} = 6.7$ mag (following Cutri et al. 2012).

When using the TGAS parallaxes, we consider only the quoted statistical uncertainties. We will show that these appear to be, if anything, slight overestimates of the uncertainty.

The posterior pdf (equation 3) is calculated on an grid of isochrones at metallicities as given in Table 2 and ages spaced by $\delta\log_{10}(\tau/\text{yr}) = 0.04$ for $\tau < 1$ Gyr and $\delta\log_{10}(\tau/\text{yr}) = 0.01$ for $\tau > 1$ Gyr. For each of these isochrones we take grid points in initial mass $\mathcal{M}$ such that there is no band in which any magnitude changes by more than 0.005 mag. We then evaluate the posterior on an informed grid in $\log A_V$ and distance, which is centred on the expected $\log A_V$ from the prior at an estimated distance (given the observed and model J-band magnitude) and then the estimated distance (given each $\log A_V$ value evaluated).

Where stars have been observed more than once by RAVE, we provide distance estimates for the quoted values from each spectrum. We provide a flag 'flag_dup' which is 0 if the spectrum is the best (or only) one for a given star, as measured by the signal-to-noise ratio, and 1 otherwise. Where one wishes to avoid double counting stars one should only use rows where this flag is 0.[2]

2.1 Standard prior

For our standard results, we use the prior that was used for DR4 and DR5. We do this for consistency, and because we find that this provides good results. The prior reflects some elements of our existing understanding of the Galaxy, at the cost of possibly biasing us against some results that run counter to our expectations (for example, metal-rich or young stars far from the plane). In Section 5 we consider alternative priors. Although the prior is described in Binney et al. (2014), we describe it here for completeness, and to enable comparisons with alternative priors considered.

The prior considers all properties in our model, and can be written as

$$\begin{aligned} P(\text{model}) &= P(\mathcal{M}, \tau, [M/H], s, A_V|l, b) \\ &= P(\mathcal{M}) \times P(A_V|s, l, b) \times P(s, [M/H], \tau|l, b) \quad (7) \end{aligned}$$

---

[2]We have based this on the RAVEID number for each source. It is worth noting that the cross-matching of stars is not perfect, and so despite our best attempts to clean duplicate entries, there may be a few per cent of stars that are in fact listed twice.

with the prior on initial mass being a Kroupa (2001) initial mass function (IMF), as modified by Aumer & Binney (2009)

$$P(\mathcal{M}) \propto \begin{cases} 0 & \text{if } \mathcal{M} < 0.1\,\text{M}_\odot \\ \mathcal{M}^{-1.3} & \text{if } 0.1\,\text{M}_\odot \le \mathcal{M} < 0.5\,\text{M}_\odot, \\ 0.536\,\mathcal{M}^{-2.2} & \text{if } 0.5\,\text{M}_\odot \le \mathcal{M} < 1\,\text{M}_\odot, \\ 0.536\,\mathcal{M}^{-2.519} & \text{otherwise.} \end{cases} \quad (8)$$

We describe extinction in terms of the value A_V for the Johnson V band, and, since extinction is necessarily non-negative, we take our prior to be Gaussian in $\ln A_V$ around an expected value which varies with the model star's position in the Galaxy, $\ln A_V^{\text{pr}}(s, l, b)$.

To find the expected value $A_V^{\text{pr}}(s, l, b)$ we start from an expected value at infinity, $A_V^{\text{pr}}(\infty, l, b)$, which we take from the Schlegel, Finkbeiner & Davis (1998) values of $E(B - V)$, with a correction for high extinction sightlines following Arce & Goodman (1999) and Sharma et al. (2011), leaving us with

$$A_V^{\text{pr}}(\infty, l, b) = 3.1 \times E(B - V)_{\text{SFD}} \{0.6 + 0.2$$
$$\times \left[1 - \tanh\left(\frac{E(B - V)_{\text{SFD}} - 0.15}{0.3} \right) \right] \}. \quad (9)$$

We then determine the expected extinction at a given distance s in the direction l, b, which is some fraction of the total extinction along that line of sight. We take this to be the fraction of the total extinguishing material along that line of sight that lies closer than s in a 3D dust model of the Milky Way taken from Sharma et al. (2011). For details of the model see Binney et al. (2014).

As in Binney et al. (2014) we take the uncertainty in $\ln A_V$ to be $\sqrt{2}$. We can then write the prior on A_V to be

$$P(A_V | s, l, b) = G(\ln A_V, \ln(A_V^{\text{pr}}(s, l, b)), \sqrt{2}). \quad (10)$$

Extinction varies between different photometric bands. For a given extinction value A_V, from Rieke & Lebofsky (1985) we take the extinctions to be

$$A_J = 0.282 A_V$$
$$A_H = 0.175 A_V$$
$$A_{K_s} = 0.112 A_V, \quad (11)$$

and, following from this, and using the results of Yuan, Liu & Xiang (2013), we have extinction in the WISE photometric bands of

$$A_{W1} = 0.0695 A_V$$
$$A_{W2} = 0.0549 A_V. \quad (12)$$

The other term in the prior is related to the probability of there being a star of a given τ, [M/H], and position. It also contains a factor of s^2, to reflect the conical shape of the surveyed volume.[3]

The prior on distance, [M/H], and age can then be written as

$$P(s, [\text{M/H}], \tau | l, b) \propto s^2 \sum_{i=1}^{3} N_i P_i([\text{M/H}]) P_i(\tau) P_i(\mathbf{r}), \quad (13)$$

where $i=$ 1, 2, 3 correspond to a thin disc, thick disc, and stellar halo, respectively, and where $\mathbf{r}$ is the Galactocentric position of the star. We then have

---

[3]This factor was stated by Burnett & Binney (2010), but not directly noted by either Burnett et al. (2011) or Binney et al. (2014), who simply stated the density profile associated with the prior on position. This oversight meant that Santiago et al. (2016) noted the absence of this factor as a difference between the Binney et al. (2014) values and their own, closely related, results. The factor of s^2 was, however, used in all of these studies.

Thin disc (i = 1):

$$P_1([\text{M/H}]) = G([\text{M/H}], 0, 0.2),$$
$$P_1(\tau) \propto \exp(0.119\,\tau/\text{Gyr}) \quad \text{for } \tau \le 10\,\text{Gyr},$$
$$P_1(\mathbf{r}) \propto \exp\left(-\frac{R}{R_d^{\text{thin}}} - \frac{|z|}{z_d^{\text{thin}}} \right); \quad (14)$$

Thick disc (i = 2):

$$P_2([\text{M/H}]) = G([\text{M/H}], -0.6, 0.5),$$
$$P_2(\tau) \propto \text{uniform in range } 8 \le \tau \le 12\,\text{Gyr},$$
$$P_2(\mathbf{r}) \propto \exp\left(-\frac{R}{R_d^{\text{thick}}} - \frac{|z|}{z_d^{\text{thick}}} \right); \quad (15)$$

Halo (i = 3):

$$P_3([\text{M/H}]) = G([\text{M/H}], -1.6, 0.5),$$
$$P_3(\tau) \propto \text{uniform in range } 10 \le \tau \le 13.7\,\text{Gyr},$$
$$P_3(\mathbf{r}) \propto r^{-3.39}; \quad (16)$$

where R signifies Galactocentric cylindrical radius, z cylindrical height, and r spherical radius. We take $R_d^{\text{thin}} = 2600\,\text{pc}$, $z_d^{\text{thin}} = 300\,\text{pc}$, $R_d^{\text{thick}} = 3600\,\text{pc}$, $z_d^{\text{thin}} = 900\,\text{pc}$. These values are taken from the analysis of SDSS data in Jurić et al. (2008). The metallicity and age distributions for the thin disc come from Haywood (2001) and Aumer & Binney (2009), while the radial density of the halo comes from the 'inner halo' detected in Carollo et al. (2010). The metallicity and age distributions of the thick disc and halo are influenced by Reddy (2010) and Carollo et al. (2010). The halo component tends towards infinite density as $r \to 0$, so we apply an arbitrary cut-off for $r < 1\,\text{kpc}$ – a region which the RAVE sample does not, in any case, probe.

The normalizations N_i were then adjusted so that at the Solar position, taken as $R_0 = 8.33\,\text{kpc}$ (Gillessen et al. 2009), $z_0 = 15\,\text{pc}$ (Binney, Gerhard & Spergel 1997), we have number density ratios $n_2/n_1 = 0.15$ (Jurić et al. 2008), $n_3/n_1 = 0.005$ (Carollo et al. 2010).

3 COMPARISON OF DR5 AND TGAS PARALLAXES

For RAVE DR5 the distance estimation used the 2MASS J, H, and K_s values, and the T_{eff}, $\log g$, and [M/H] values calculated from RAVE spectra. The parallaxes computed were compared with the parallaxes obtained by the *Hipparcos* mission (Perryman et al. 1997), specifically those found by the new reduction of van Leeuwen (2007) for the ~5000 stars common to both catalogues. The parallaxes were compared by looking at the statistic

$$\Delta = \frac{\langle \varpi_{\text{sp}} \rangle - \varpi_{\text{ref}}}{\sqrt{\sigma_{\varpi, \text{sp}}^2 + \sigma_{\varpi, \text{ref}}^2}}, \quad (17)$$

where ϖ_{sp} and $\sigma_{\varpi, \text{sp}}$ are the spectrophotometric parallax estimates and their uncertainties, respectively. In Kunder et al. (2017) the reference parallax ϖ_{ref} and its uncertainty $\sigma_{\varpi, \text{ref}}$ were from *Hipparcos*, but henceforth in this paper they will be from TGAS. A negative value of Δ, therefore, corresponds to an overestimate of distance from RAVE (compared to the reference parallaxes), and a positive value corresponds to an underestimate of distance. We

would hope that the mean value of Δ is zero and the standard deviation is unity (consistent with the uncertainties being correctly estimated).

Here, as in Kunder et al. (2017) we divide the stars into dwarfs ($\log g \geq 3.5$) and giants ($\log g < 3.5$), and further subdivide dwarfs into hot ($T_{\mathrm{eff}} > 5500\,\mathrm{K}$) and cool ($T_{\mathrm{eff}} \leq 5500\,\mathrm{K}$). It is worth noting that this means that main-sequence turn-off stars are likely to be put in the 'dwarf' category. In Fig. 2 we show a comparison between the DR5 parallaxes and the TGAS parallaxes described by this statistic (which we call $\Delta_{\mathrm{DR5\text{-}TGAS}}$ in this case). The figures show kernel density estimates (KDEs; Scott 1992), which provide an estimate of the pdf of Δ_{DR5} for each group, along with finely binned histograms (which are used to give a sense of the variation around the smooth KDE). These are generally encouraging for both cool dwarfs and giants, with a mean value that is close to zero (meaning that any parallax, and therefore distance, bias is a small fraction of the uncertainty), and a dispersion that is slightly smaller than unity (implying that the uncertainties of one or both measurements are overestimated).

For hot dwarfs there is a clear difference between the DR5 parallaxes and the TGAS parallaxes. The mean value of Δ is 0.301, meaning that the systematic error in parallax is a significant fraction of the uncertainty, with the DR5 parallaxes being systematically larger than the TGAS parallaxes (corresponding to systematically smaller distance estimates from DR5).

The typical combined quoted uncertainty on the parallaxes for hot dwarfs is ~1 mas, so this systematic difference is ~0.3 mas, which is comparable to the size of the colour-dependent and spatially correlated uncertainties identified by Lindegren et al. (2016). It was therefore not immediately obvious whether the difference seen here is due to a systematic error with the DR5 parallaxes, or with the TGAS parallaxes.

However, we have indications from Kunder et al. (2017) that the effective temperatures found by the RAVE pipeline tend to be underestimates for $T_{\mathrm{eff}} \gtrsim 5300\,\mathrm{K}$. The effective temperatures determined using the IRFM are systematically *higher* than those found from the RAVE pipeline (Fig. 26; Kunder et al. 2017). If the effective temperature used in the distance estimation is systematically lower than the true value, then this will cause us to systematically underestimate the luminosity of the star, and thus underestimate its distance (overestimate its parallax). Therefore, a systematic underestimate of T_{eff} by the RAVE pipeline can explain the difference with the IRFM T_{eff} values *and* the systematic difference with the TGAS parallaxes. This motivates us to investigate the IRFM temperatures in Section 4 for an improved estimate of T_{eff}, and thus more accurate distance estimates.

We can investigate this more closely by looking at how an average value of Δ_{DR5} (which we write as $\langle\Delta_{\mathrm{DR5}}\rangle$) varies with T_{eff} for dwarfs or with $\log g$ for giants. In Fig. 3 we show the running average of this quantity in windows of width 200 K in T_{eff} for dwarfs and 0.3 dex in $\log g$ for giants. For reference we also include the number density as a function of these parameters in each case.

The left-hand panel of Fig. 3 shows the value of $\langle\Delta_{\mathrm{DR5\text{-}TGAS}}\rangle(T_{\mathrm{eff}})$ for dwarfs. As we expect, we see that for $T_{\mathrm{eff}} \gtrsim 5500\,\mathrm{K}$ we have a parallax offset of ~0.3 times the combined uncertainty, which has a small dip around 7400 K.[4] The vast majority of what we termed 'cool dwarfs' are in the temperature range $4600 \lesssim T_{\mathrm{eff}} < 5500\,\mathrm{K}$, where TGAS and RAVE clearly agree nicely.

Below ~4600 K the value of $\langle\Delta\rangle(T_{\mathrm{eff}})$ goes to very large values, corresponding to a substantial underestimate of distance by RAVE DR5. This was not clearly seen in Fig. 2 because there are very few dwarfs in this temperature range. It is not clear what causes this, though it could occur if (1) there is a tendency to underestimate the T_{eff} for these stars, which is not something which has been noted before; (2) stars with quoted $\log g$ values between the dwarf and giant branches have been given too high a probability of being dwarfs by the pipeline, and/or (3) the pipeline assigns too low a luminosity to stars near this part of the main sequence – possibly because many of them are still young and perhaps still settling on to the main sequence (see Žerjal et al. 2017).

The right-hand panel of Fig. 3 shows the value of $\langle\Delta_{\mathrm{DR5}}\rangle(\log g)$ for giants. In the range $2.2 \lesssim \log g \lesssim 3.0$ (which is a region with a high number of stars) we can see that the DR5 parallaxes more or less agree with those from TGAS. However, at high $\log g$ RAVE parallaxes are on average larger than those from TGAS (corresponding to an underestimate of the luminosity), whereas at low $\log g$ RAVE parallaxes are on average smaller than those from TGAS (i.e. the luminosity is overestimated). We will discuss this difference in Section 4.1.

It is worth emphasizing that the effects we see here for low T_{eff} or low $\log g$ are not ones that we would simply expect to be caused by the statistical uncertainties in the RAVE parameters (e.g. the stars with the lowest quoted $\log g$ values being only the ones scattered there by measurement error). The Bayesian framework compensates for exactly this effect, so the problem we are seeing is real.

4 USING OTHER RAVE DATA PRODUCTS FOR DISTANCE ESTIMATION

We now look at how the difference between parallaxes derived from RAVE and those from TGAS compare if we use T_{eff} values derived from the IRFM, rather than those derived from the spectrum directly. We also include WISE photometry in the *W1* and *W2* bands in both cases (as discussed in Section 2).

Fig. 4 again shows the difference between the parallaxes we derive and those found by TGAS, divided into the same three categories. We can see that the disagreement for hot dwarfs is significantly reduced from that found for DR5, with a systematic offset that is half that seen when using the spectroscopic T_{eff} values. However, we can also see that the agreement between the two values is now slightly less good than before for cool dwarfs and for giants.

We can explore this in more detail by, again, looking at how the average value of Δ varies as we look at different T_{eff} for all dwarfs. In Fig. 5 we show how a running average, $\langle\Delta\rangle(T_{\mathrm{eff}})$, varies for dwarfs when we use the IRFM or the spectroscopic T_{eff} values.[5] It is clear that whatever we choose as a T_{eff} value, our parallax estimates differ dramatically from those from TGAS for dwarfs with $T_{\mathrm{eff}} \lesssim 4600\,\mathrm{K}$, but there are very few dwarfs with these temperatures. For $4600\,\mathrm{K} \lesssim T_{\mathrm{eff}} \lesssim 5500\,\mathrm{K}$ the values found using the spectroscopically determined T_{eff} values are better than those found using the IRFM values, while for $T_{\mathrm{eff}} \gtrsim 5500\,\mathrm{K}$ the IRFM values are better. Even using the IRFM temperatures, the parallaxes found at $T_{\mathrm{eff}} \sim 6400\,\mathrm{K}$ are still somewhat larger than those found by TGAS.

---

[4]The sharp edges are due to the fact that a relatively large number of sources are assigned temperatures very near to 7410 K, due to the pixelization produced by the fitting algorithm – see Kordopatis et al. (2011).

[5]Note that the $\langle\Delta\rangle$ values using the spectroscopic T_{eff} values are now not those given in DR5, but new ones, found when we include the WISE photometry. These prove to be very similar to those found by DR5.
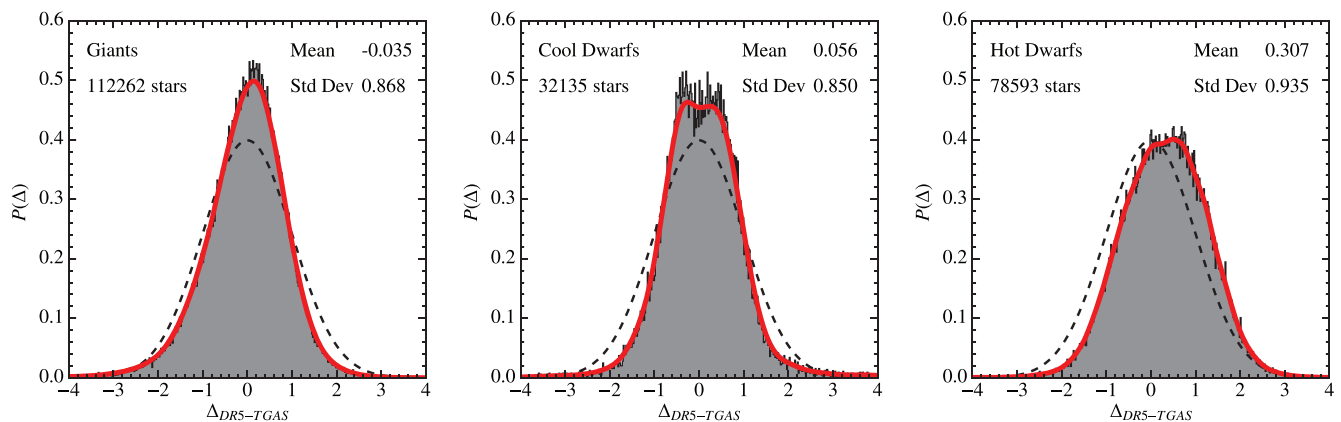
Figure 2. Comparison of parallax estimates from RAVE DR5 and those from TGAS. We divide the stars into giants ($\log g < 3.5$), cool dwarfs ($\log g \geq 3.5$ and $T_{\rm eff} \leq 5500$ K), 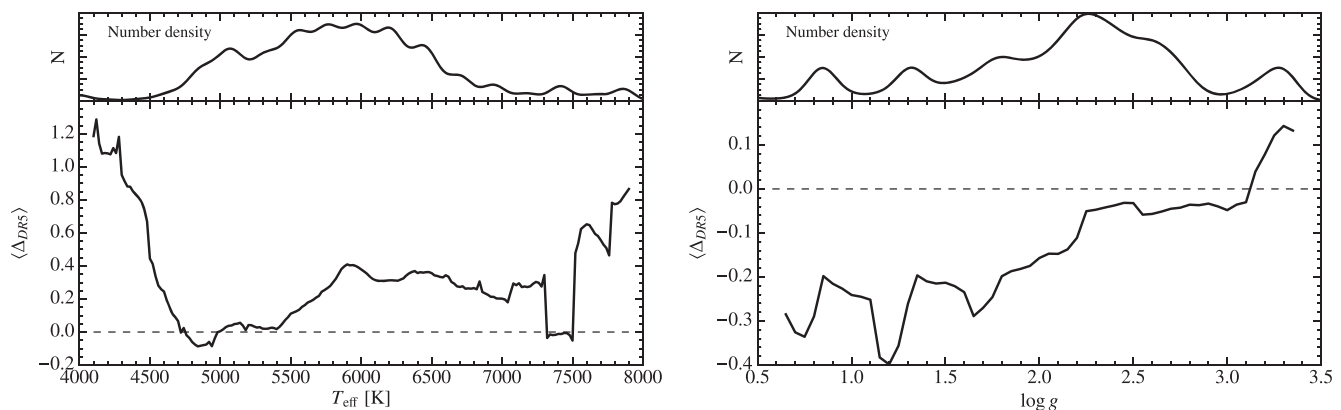and hot dwarfs ($\log g \geq 3.5$ and $T_{\rm eff} > 5500$ K) and provide pdfs of Δ (i.e. difference between spectrophotometric parallax and TGAS parallax, normalized by the combined uncertainty, see equation 17) in each case. The *red* lines show the kernel density estimate of this pdf in each case, with the finely binned grey histogram shown to give an indication of the variation around this smooth estimate. The *black dashed line* is a Gaussian with a mean 0 and standard deviation of unity. The means and standard deviations shown in the top right are for stars with $-4 < \Delta_{\rm DR5} < 4$, to avoid high weight being given to outliers. Positive values of Δ correspond to parallax overestimates (i.e. distance or luminosity underestimates).

Figure 3. Running average of Δ (i.e. difference between spectrophotometric parallax and TGAS parallax, normalized by the combined uncertainty; see equation 17) as a function of $T_{\rm eff}$ for dwarfs (left lower) and $\log g$ for giants (right lower), comparing DR5 values to those from TGAS. The running averages are computed for widths of 200 K and 0.3 dex, respectively. The plot also shows the number density as a function of $T_{\rm eff}$ and $\log g$, respectively, for reference. Means are only calculated for stars with $-4 < \Delta_{\rm DR5\text{-}TGAS} < 4$. Note that positive values of Δ correspond to parallax overestimates (i.e. distance or luminosity underestimates).

4.1 Giants

We can now turn our attention to the giant stars. When we simply divide the stars into dwarfs and giants – as was done with *Hipparcos* parallaxes by Binney et al. (2014) and Kunder et al. (2017), and with TGAS parallaxes in Figs 2 and 4 of this study – any biases appear small. However, when we study the trend with $\log g$, as in Figs 3 and 6, we see that while the stars with $\log g \gtrsim 2.2$ have RAVE parallaxes that are very similar to those from TGAS (with a moderate overestimate for $\log g < 3$), the stars with lower $\log g$ values have RAVE parallaxes which seem to be systematically underestimated (corresponding to distance overestimates).

We can understand how this may have come about if we look at the comparison of the RAVE $\log g$ values with those found by GALAH (Martell et al. 2017) or APOGEE (Wilson et al. 2010) for the same stars – as presented in figs 17 and 19 of Kunder et al. (2017). In both cases there appears to be a trend that the other surveys find larger $\log g$ values for stars assigned RAVE $\log g \lesssim$

2. A systematic underestimate of the $\log g$ values of these stars would lead to exactly this effect. In Section 4.1.1 we will look at the asteroseismic re-calibration of RAVE $\log g$ found by Valentini et al. (2017), which also suggests that these $\log g$ values may be underestimated.

It is important to note that these low $\log g$ stars are intrinsically luminous, and therefore those observed by RAVE tend to be distant. This means they have relatively small parallaxes, and so the quoted TGAS uncertainties are a large fraction of true parallax, while those from RAVE are relatively small. Fig. 7 illustrates this point by showing the median parallax and uncertainty for each method as a function of $\log g$.

A consequence of this is that the combined parallax uncertainty used to calculate Δ is dominated by that from TGAS. We illustrate this in Fig. 8, which shows the median value of the alternative statistic $(\varpi_{\rm IRFM} - \varpi_{\rm TGAS})/\sigma_{\varpi,\rm IRFM}$, where $\varpi_{\rm IRFM}$ is the parallax estimate using the IRFM $T_{\rm eff}$ value, and $\sigma_{\varpi,\rm IRFM}$ is the corresponding
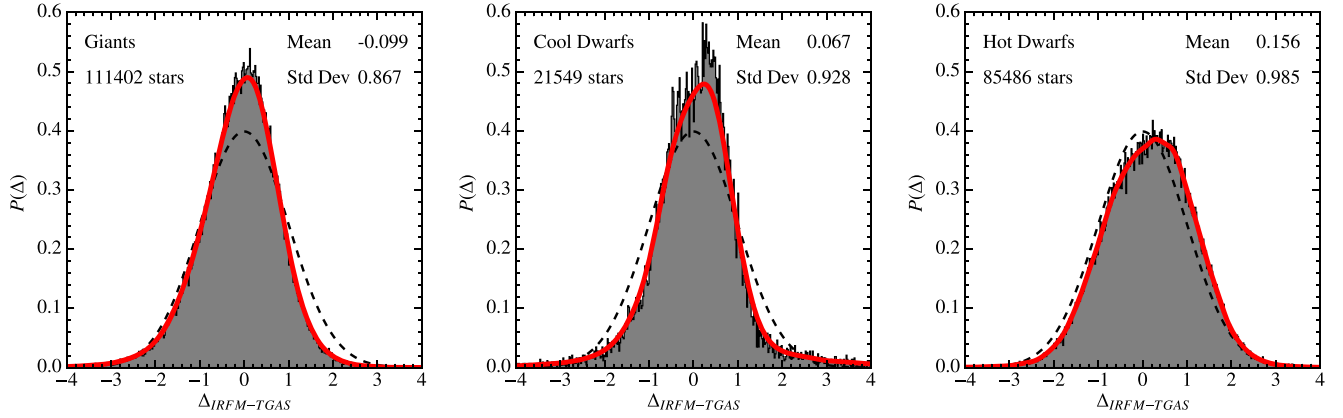
Figure 4. Comparison of parallax estimates from RAVE with temperatures taken from the IRFM and parallax measurements from TGAS. This plot shows the same statistics as in Fig. 2, and again we divide the stars into giants ($\log g < 3.5$), cool dwarfs ($\log g \geq 3.5$ and $T_{\rm eff,\,IRFM} \leq 5500\,\rm K$), and hot dwarfs ($\log g \geq 3.5$ and $T_{\rm eff,\,IRFM} > 5500\,\rm K$) and provide pdfs of Δ (equation 17) in each case – positive values of Δ correspond to parallax overestimates (i.e. distance or luminosity underestimates). The main difference we can see is that the parallax estimates for hot dwarfs are substantially improved.
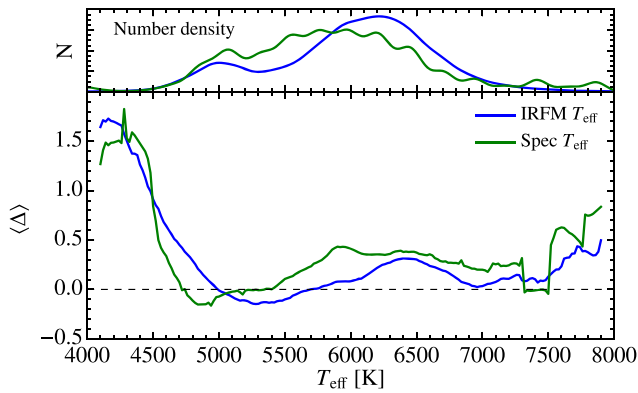
Figure 5. As Fig. 3 (left-hand panel), this is a running average of Δ as a function of $T_{\rm eff}$ for dwarfs ($\log g \geq 3.5$), but here we are using $T_{\rm eff}$ values determined by the IRFM (blue) or from the RAVE spectra (green). Again, the plot also shows the number density of dwarfs as a function of $T_{\rm eff}$ for reference. Use of the IRFM temperatures reduces the bias seen for hot dwarfs.

Figure 7. Median parallax (solid line) and median parallax uncertainty (shaded region) for the RAVE pipeline using IRFM $T_{\rm eff}$ values (blue) and TGAS (red) as a function of $\log g$. The quoted parallax uncertainty from RAVE becomes much smaller than that from TGAS as $\log g$ becomes small. This means that when we use the TGAS parallaxes to improve the distance estimates, they will have little influence at the low $\log g$ end.

Figure 6. As Fig. 3 (right-hand panel), this is a running average of Δ as a function of $\log g$ for giants ($\log g < 3.5$), but here we are using $T_{\rm eff}$ values determined by the IRFM (blue) or from the RAVE spectra (green). Again, the plot also shows the number density as a function of $\log g$, respectively, for reference. Means are calculated for stars with $-4 < \Delta < 4$.
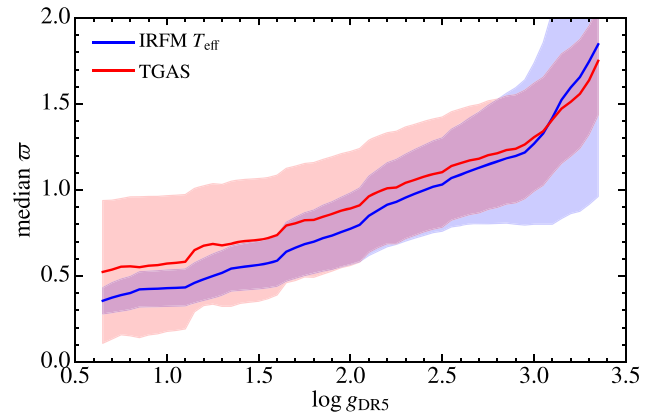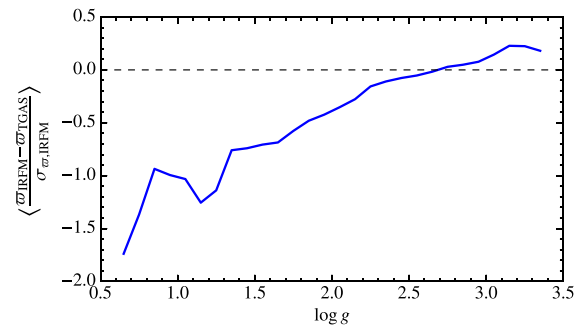

Figure 8. Running average of $(\varpi_{\rm IRFM} - \varpi_{\rm TGAS})/\sigma_{\varpi,\rm IRFM}$ as a function of $\log g$ for giants ($\log g < 3.5$) – this statistic is similar to Δ used elsewhere, but does not include the TGAS uncertainty. It therefore shows the typical systematic offset of the RAVE parallax estimates as a function of the quoted uncertainty. For the lowest $\log g$, the two values are comparable.

uncertainty.[6] This shows that the systematic error for the lowest $\log g$ stars is comparable to the quoted statistical uncertainty.

This also means that when we include the TGAS parallaxes in the distance pipeline for these objects, it will typically have a rather limited effect, and so the bias that we see here will persist.

4.1.1 Asteroseismic calibration

The $\log g$ values given in the main table of RAVE DR5 have a global calibration applied, which uses both the asteroseismic $\log g$ values of 72 giants from Valentini et al. (2017) and those of the *Gaia* benchmark dwarfs and giants (Heiter et al. 2015). This leads to an adjustment to the raw pipeline values (which were used in RAVE DR4, so we will refer to them as $\log g_{DR4}$) such that

$$\log g_{DR5} = \log g_{DR4} + 0.515 - 0.026 \times \log g_{DR4}$$
$$- 0.023 \times \log g_{DR4}^2. \qquad (18)$$

A separate analysis was carried out by Valentini et al. (2017) which focused only on the 72 giants with asteroseismic $\log g$ values, which are only used to recalibrate stars with dereddened colours $0.50 < (J - K_s)_0 < 0.85$ mag, and they found that for these stars a much more drastic recalibration was preferred, with the recalibrated $\log g$ value being

$$\log g_{AS} = \log g_{DR4} - 0.78 \log g_{DR4} + 2.04$$
$$\approx 2.61 + 0.22 \times (\log g_{DR4} - 2.61). \qquad (19)$$

This has the effect of increasing the $\log g$ values for stars in the red clump and at lower $\log g$ – thus decreasing their expected luminosity and distance, and increasing their expected parallax. It has the opposite effect on stars at higher $\log g$. It is clear, therefore, that this recalibration is in a direction required to eliminate the trend in Δ with $\log g$ for giants seen in the right-hand panel of Fig. 3. It is also worth noting that Kunder et al. (2017) compared $\log g_{AS}$ to literature values and found a clear trend in the sense that $\log g_{AS}$ was an overestimate for stars with literature $\log g < 2.3$, and an underestimate for literature $\log g > 2.8$.

In Fig. 9 we show Δ as a function of $\log g_{DR5}$ for stars using the recalibrated $\log g_{AS}$ values given by Valentini et al. (2017) (along with those when using the DR5 $\log g$ values for reference). We use the DR5 $\log g$ value on the x-axis to provide a like-for-like comparison, and the grey region in Fig. 9 is equivalent to the range $2.3 < \log g_{AS} < 2.8$. It is clear that the asteroseismically calibrated $\log g$ values improve the distance estimation for stars with low $\log g$ values – even beyond the range of $\log g$ values where these $\log g$ values disagree with other external catalogues (as found by Kunder et al. 2017) – though it should be noted that these stars [with $0.50 < (J - K_s)_0 < 0.85$ mag] represent a small fraction of the stars with these low $\log g$ values.

However, for gravities greater than $\log g_{DR5} \simeq 2.5$ (which is the point where $\log g_{AS} = \log g_{DR5}$), the asteroseismic calibration makes the $\log g$ values significantly worse in the sense that the spectrophotometric parallaxes are underestimates (i.e. the distances are typically overestimated). Inspection of the comparison of RAVE DR5 $\log g$ values to those from GALAH or APOGEE in Kunder et al. (2017) appears to indicate that those with $\log g_{DR5} \approx 3$ are split into two groups (one with higher $\log g$ found by the other surveys, one with lower) – i.e. these are a mixture of misidentified
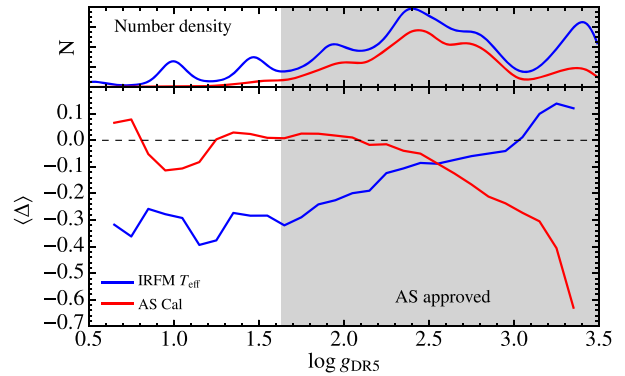
Figure 9. As Fig. 6 this is a running average of Δ as a function of $\log g_{DR5}$ for giants where the $\log g$ values used come from the main DR5 calibration (blue; equation 18) or the asteroseismic calibration (red; equation 19). Note that the x-axis gives the DR5 $\log g$ value in each case – this is to enable a side-by-side comparison. In both cases we have used T_{eff} values determined by the IRFM. The grey region indicates the range in $\log g$ over which the asteroseismic calibration appears to work reasonably well for the reference stars considered by Kunder et al. (2017). The running averages are computed for over a width of 0.3 in $\log g$. The plot also shows the number density as a function of $\log g$, respectively, for reference. Means are calculated for stars with $-4 < \Delta < 4$. Using the asteroseismically calibrated $\log g$ values for stars clearly improves the distance estimates for $\log g_{DR5} \lesssim 2.5$, which is the point where the two values are equal, but makes them worse for $\log g_{DR5} \gtrsim 2.5$.

dwarfs/subgiants and giants. The asteroseismic calibration is blind to this difference, and it seems likely that it does a reasonable job of correcting the $\log g$ values for the giants, at the cost of dramatically underestimating the $\log g$ values for the dwarfs/subgiants at the same $\log g_{DR5}$.

The Valentini et al. (2017) catalogue comes with an entry 'flag_050' which is true if the difference between $\log g_{DR5}$ and $\log g_{AS}$ is less than 0.5, and it is recommended that only stars with this flag are used. This sets an upper limit of $\log g_{DR5} \simeq 3.5$ for sources where the asteroseismic calibration can be applied. Our work here implies that the asteroseismic calibration should not be used for sources with $\log g_{DR5} \gtrsim 2.7$.

4.2 Outliers

We have ~ 1000 stars for which the quoted parallaxes from RAVE and TGAS differ by more than 4σ. We will refer to these as 'outliers'. We would only expect ~ 12 such objects if the errors were Gaussian with the quoted uncertainties. In Fig. 10 we show pdfs indicating how these stars are distributed in quoted $T_{eff, IRFM}$, $\log g$, and [M/H]. They cover a wide range of these parameters, and no clear problematic area is evident. They do tend to have relatively low T_{eff} values, and constitute a relatively large fraction of stars with quoted [M/H] values towards either end of the full range.

We also show the distribution of these stars in terms of S/N, and we can see that while they tend to have relatively low S/N values, they are certainly not limited to such stars. We have also looked at the values of the AlgoConv quality flag, which is provided with RAVE parameters, and find that the outliers are indicated as unreliable around the same rate as the rest of the sources. Around 26 per cent of the outliers have flags 2 or 3, which indicate that the stellar parameters should be used with caution, as compared to ~ 23 per cent of all other sources, which suggests that this is not the problem.
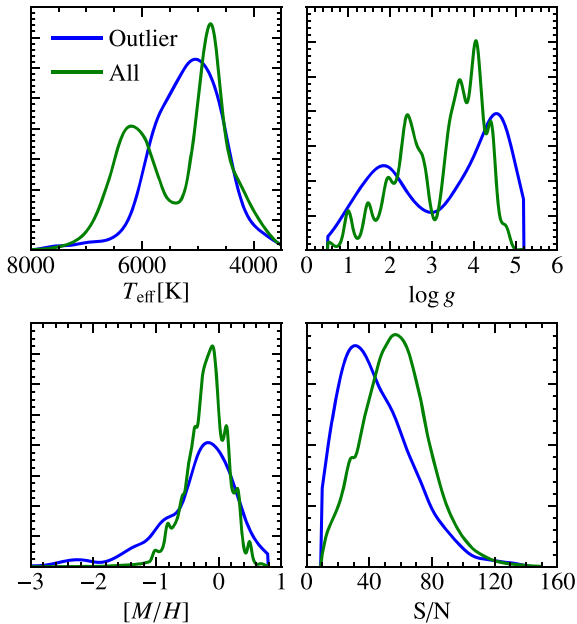
Figure 10. Distributions of the quoted parameters of the ~1000 stars that are outliers in the sense that they have $|\Delta| > 4$ (*blue* lines), and of all stars in the study, for reference (*green* lines). The plots are pdfs (so the area is normalized to 1 in all cases) produced using a kernel density estimate. The distributions shown are in $T_{\mathrm{eff,\ IRFM}}$ (top left), $\log g_{\mathrm{DR5}}$ (top right), [M/H] (bottom left), and *S/N* (bottom right). The outliers cover a wide range of these parameter spaces, and do not come from any clearly distinct population.

There is also no indication that they are particularly clustered on the sky.

There is some indication that the outliers tend to be problematic sources as labelled by the flags from Matijevič et al. (2012), which are provided with DR5. These flags are based on a morphological classification of the spectra, and can indicate that stars are peculiar (e.g. have chromospheric emission or are carbon stars) or that the spectra have systematic errors (e.g. poor continuum normalization). ~20 per cent of the outliers are flagged as binary stars, and ~35 per cent are flagged as having chromospheric emission (compared to ~2 per cent and ~6 per cent of all sources, respectively). Similarly, ~40 per cent of the outliers are in the catalogue of stars with chromospheric emission from Žerjal et al. (2013, 2017). The chromospheric emission can only have affected the RAVE distance estimates. However, binarity can affect either the RAVE distance (by affecting the parameter estimates and/or observed magnitudes) or the TGAS parallaxes (by altering the star's path across the sky, thus changing the apparent parallax).

4.3 Metallicity

Finally, we can look at the variation of Δ with more than one stellar parameter. In Fig. 11 we show the variation of Δ in the Hertzsprung–Russell (HR) diagram (T_{eff} against $\log g$) for all stars. We also show the variation of Δ in the [M/H]–T_{eff} plane for dwarfs and the [M/H]–$\log g$ plane for giants. In all cases we just show the statistics when we use the IRFM temperatures.

The HR diagram shows some areas where RAVE parallaxes appear to be particularly discrepant. We had already seen that low-temperature dwarfs ($T_{\mathrm{eff,\ IRFM}} \lesssim 4500$ K) have overestimated parallaxes. The sources with $T_{\mathrm{eff,\ IRFM}} \sim 5000$ K and $\log g_{\mathrm{DR5}} \sim 4.2$ have underestimated parallaxes. These sources are between the dwarf and

subgiant branches, and it appears that they are typically assigned too high a probability of belonging to the subgiant branch. These will be greatly improved when we include the TGAS parallax in our estimates. Sources at the upper edge of the giant branch (high quoted T_{eff} for their quoted $\log g$) also have very small RAVE parallaxes compared to those from TGAS, but these are a small fraction of giant stars.

There are no clear trends with metallicity for giants. For the dwarfs it is perhaps notable that there are significant parallax underestimates for metal-poor stars at $T_{\mathrm{eff}} \sim 5200$ K and parallax overestimates for both unusually metal-poor and metal-rich stars at $T_{\mathrm{eff}} \sim 6200$ K. Again these do not comprise a particularly large fraction of all sources, and will be corrected when we include the TGAS parallax in our estimates. It is worth noting that selection effects mean that the more metal-poor stars (which tend to be further from the Sun in the RAVE sample) are likely to be higher temperature dwarfs, and (particularly) lower $\log g$ giants, and this affects any attempts to look at variation of Δ with metallicity independent of the other stellar parameters.

Since the most metal-poor stars tend to be cool giants which, as we have noted, are assigned distances in our output that are systematically too large, a sample of our stars which focusses on the metal-poor ones will suffer from particularly serious distance overestimates. Any prior which (like our standard one) assumes that metal-poor stars are the oldest will have a similar overestimate for the stars that are assigned the oldest ages in the sample. Note, however, that the age estimates we provide are found using a prior which assumes no such age–metallicity relation (see Section 5.1), so the most metal-poor stars are not necessarily assigned the oldest ages in our catalogue.

4.4 Which to use?

It is clear that adopting the IRFM temperature estimates improves the distance estimates for stars that have $T_{\mathrm{eff,\ Spec}} > 5500$ K. Use of the IRFM temperatures does make the problems at low $\log g$ somewhat worse than they already were, but this is a smaller effect. We feel that switching from one temperature estimate to another at different points in the HR diagram would be a mistake, so we use the IRFM temperature in all cases. For ~5000 sources there is no IRFM T_{eff} available, so we do not provide distance estimates.

For sources recognized as outliers ($|\Delta| > 4$) we assume that the RAVE parameters are unreliable, in the published catalogue these are flagged, and we provide distances estimated using only TGAS parallaxes and the 2MASS and WISE photometry. Similarly, we recognize that there is a systematic problem with dwarfs at $T_{\mathrm{eff}} < 4600$ K, so for these stars we exclude the RAVE T_{eff} and $\log g$ from the distance estimation, and add an (arbitrary) 0.5 dex uncertainty in quadrature with the quoted RAVE uncertainty on metallicity.

We have seen that sources with $\log g_{\mathrm{DR5}} < 2.0$ show a systematic difference between our parallax estimates and those found by TGAS. This is probably due to a systematic underestimate of $\log g$ for these stars by RAVE. We will determine distances to these stars in the same way as to the others, but they will be flagged as probably unreliable. While the asteroseismic recalibration clearly helps for these stars, it is not helpful at high $\log g$, and is applicable to a dwindling fraction of sources as we go to lower $\log g$. We therefore do not attempt to use this recalibration in our distance estimates, though it certainly indicates the direction we must go to improve the RAVE $\log g$ estimates.
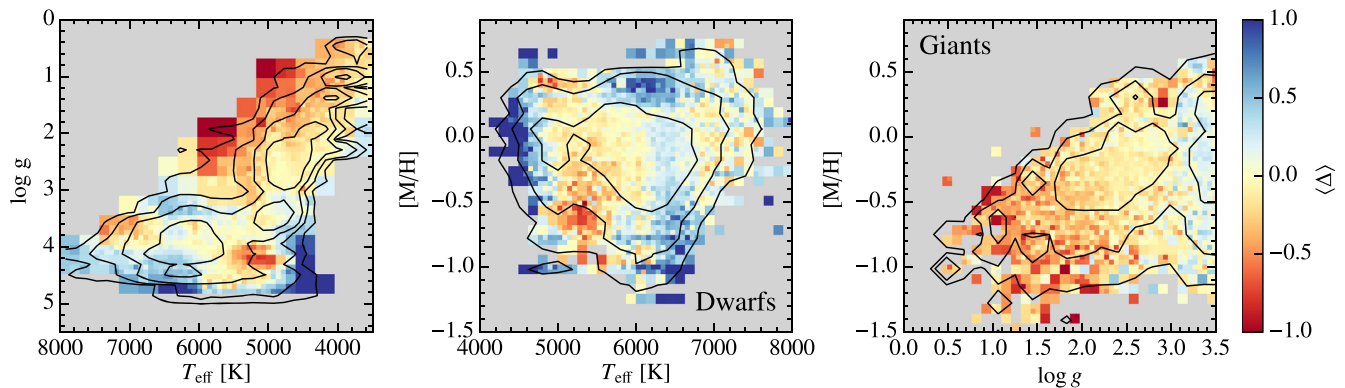
Figure 11. Median values of Δ, using IRFM temperatures, as a function of the stellar parameters $T_{\rm eff}$, log g, and [M/H]. Pixel sizes are adapted such that there is never fewer than 10 stars in a pixel for which we show the median. For the variation with metallicity we have, as before, divided the stars into dwarfs and giants, to show the more relevant parameter in each case. The grey areas contain very few stars. Density contours are shown as a guide to the location of the majority of the sources in these plots (this shows signs of the pixelization of these parameters produced by the fitting algorithm used in the RAVE spectroscopic pipeline).

5 ALTERNATIVE PRIORS

It would be very troubling if our results were strongly dependent on our choice of prior. We therefore explore the effect of our prior by considering alternative forms. We will call our standard prior 'Standard', and describe the differences from this prior. We consider four main alternative forms:

(i) 'Density' prior. As Standard, except that we set the prior on [M/H] and τ to be uniform, with a maximum age of 13.8 Gyr. The minimum and maximum metallicities are effectively set by the isochrone set used (Table 2).[7] This leaves the density profile, IMF, and dust model unchanged.

(ii) 'Age' prior. As Standard, except that the age prior is the same for all components and simply reflects the assumption that the star formation rate has declined over time, following the same functional form as for the thin disc in the Standard prior, i.e.

$$P(\tau) \propto \exp(0.119\,\tau/\mathrm{Gyr}) \quad \text{for } \tau \leq 13.8\,\mathrm{Gyr}. \tag{20}$$

(iii) 'SB14' prior. As Standard, except that we set the prior on [M/H] and τ identically for all components, following Schönrich & Bergemann (2014). This is uniform in [M/H] over the metallicity range set by the isochrones, such that

$$P(\tau\,|\,[\mathrm{M/H}]) \propto \begin{cases} 0 & \text{if } \tau > 13.8\,\mathrm{Gyr} \\ 1 & \text{if } 11\,\mathrm{Gyr} \leq \tau \leq 13.8\,\mathrm{Gyr} \\ \exp\left[\frac{(\tau - 11\,\mathrm{Gyr})}{\sigma_\tau([\mathrm{M/H}])}\right] & \text{if } \tau \leq 11\,\mathrm{Gyr}, \end{cases} \tag{21}$$

where

$$\sigma_\tau = \begin{cases} 1.5\,\mathrm{Gyr} & \text{if } [\mathrm{M/H}] < -0.9 \\ \left(1.5 + 7.5 \times \frac{0.9 + [\mathrm{M/H}]}{0.4}\right)\,\mathrm{Gyr} & \text{if } -0.9 \leq [\mathrm{M/H}] \leq -0.5 \\ 9\,\mathrm{Gyr} & \text{otherwise.} \end{cases} \tag{22}$$

(iv) 'Chabrier' prior. As Standard, except that we use a Chabrier (2003) IMF rather than a Kroupa (2001) IMF, where following

---

[7]It is possible to remove this limitation, under the assumption that the stellar models do not change much at lower or higher metallicities, but the effect is limited, and it is not implemented here.

Romano et al. (2005) we take

$$P(\mathcal{M}) \propto \begin{cases} 0 & \text{if } \mathcal{M} < 0.1\,\mathrm{M_\odot} \\ \frac{A_c}{\mathcal{M}} \exp\left(\frac{\log_{10}\mathcal{M} - \log_{10}\mathcal{M}_c}{\sigma_c}\right)^2 & \text{if } 0.1\,\mathrm{M_\odot} \leq \mathcal{M} < \mathrm{M_\odot}, \\ B_c\,\mathcal{M}^{-2.3} & \text{otherwise.} \end{cases} \tag{23}$$

In Fig. 12 we compare the values of Δ that we derive under all of these priors, in each case using the sets of input parameters described in Section 4.4, and excluding sources where we ignore the RAVE parameters.

It is clear from the left-hand panel of Fig. 12 that the priors make a very limited difference for the dwarfs, except at the low $T_{\rm eff}$ end, where contamination by giants is becoming more important.

The right-hand panel of Fig. 12 shows that for giants, a prior that is uniform in both [M/H] and stellar age – i.e. the Density prior – provides even worse results for the low log g giants than the Standard prior. The other priors provide very similar results to one another at low log g, but differ somewhat at the higher log g end – the two priors, where $P([\mathrm{M/H}])$ is a function of position (Standard and Chabrier), tend to have lower Δ values, i.e. greater distances to these stars derived from RAVE.

We have also explored the effect of changing the power-law slope of the halo within our Standard prior (equation 16) to either $P_3(\mathbf{r}) \propto r^{-3.9}$ or $P_3(\mathbf{r}) \propto r^{-2.5}$ (compared to the usual $r^{-3.39}$). The results were essentially indistinguishable from those using the Standard prior, even if we isolate the metal-poor stars. Similarly, a decrease of 50 per cent for the thin and thick disc scale heights has almost no effect – the mean and standard deviations of the Δ values for a given population of stars (as shown in, e.g. Fig. 4) change by $\sim$0.001 at most.

5.1 Choice of prior

In the interests of consistency with past studies, we use the Standard prior when producing our distance estimates. However, it is clear that this choice of prior imposes a strong relationship between age and metallicity. Therefore, we also provide age estimates (Section 8) using our 'Age' prior. The results presented in this section make it clear that results using this prior are roughly as reliable as those from our Standard prior, at least in terms of typical parallax error.
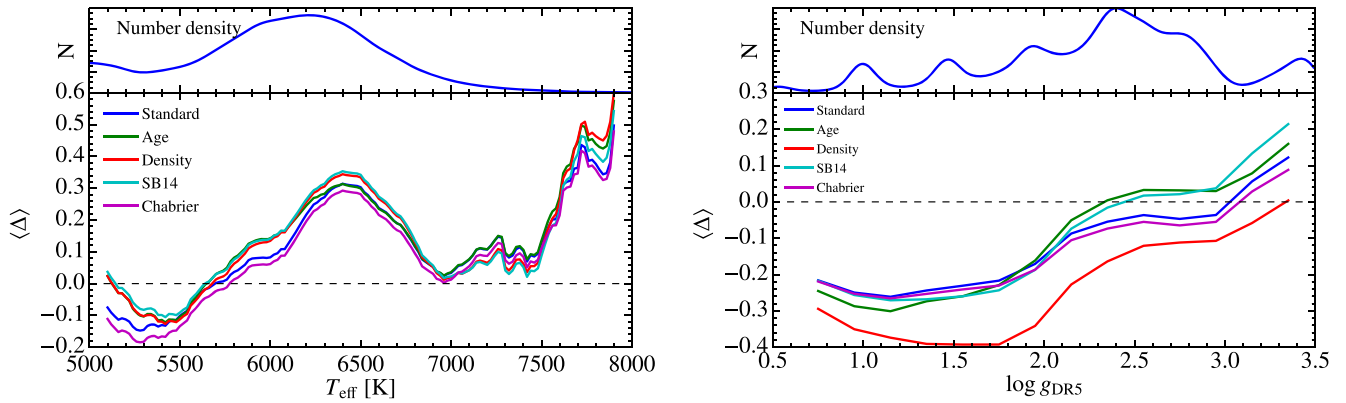
Figure 12. As Fig. 3, this is the running average of Δ as a function of T_{eff} for dwarfs (left lower) and $\log g$ for giants (right lower) when using the alternative priors described in Section 5. In general, the RAVE distance estimates are reasonably robust to a change of prior.

6 USING RAVE PARALLAXES TO LEARN ABOUT TGAS

In Section 4 we used the TGAS parallaxes to investigate the RAVE distance estimation, but we can turn this around and use the RAVE distance estimation to learn about TGAS. TGAS is an early release of *Gaia* data and is therefore expected to contain strong systematic errors (Gaia Collaboration 2016b; Lindegren et al. 2016). Various studies have looked at these systematic errors (including the *Gaia* consortium itself: Arenou et al. 2017), by comparison to distances derived for RR Lyrae stars (Gould et al. 2016), red clump stars (Davies et al. 2017; Gontcharov & Mosenkov 2017), or eclipsing binaries (Stassun & Torres 2016) or, in the case of Schönrich & Aumer (2017), using a statistical approach based on the correlations between velocity components produced by distance errors. Our approach allows us to study a large area in the southern sky using many sources, spanning a wide range in colour, without any assumptions about kinematics.

In Fig. 13 we plot the average difference between the TGAS parallax and that from this study, binned on the sky. Zonal differences are unlikely to be produced by any particular issues with the RAVE distance estimation, but may be related to the way in which the sky has been scanned by *Gaia*. We can clearly see a stripe showing a substantial difference at $l \sim 280°$, which corresponds to a stripe near the ecliptic pole, as can be seen when this diagram is shown in ecliptic coordinates. A similar figure was shown in Arenou et al. (2017, fig. 28), using the RAVE DR4 parallax estimates, where this feature was attributed to the 'ecliptic scanning law followed early in the mission', and it was noted that a corresponding feature can be found in the median parallaxes of quasar sources. This is also likely to be related to the anomaly reported by Schönrich & Aumer (2017).

We can also look again at the width of the distribution of Δ. As we have seen already, the width of the distribution of Δ, when comparing TGAS and DR5, is less than unity. In Fig. 14 we show this width for all stars in our new RAVE-only parallax estimates, and it is again less than unity. This indicates that the uncertainties of one or other measurements have been overestimated. When we divide the distribution by quoted TGAS parallax uncertainty (Fig. 15) we can see that the problem is particularly acute for sources with small quoted TGAS uncertainties.

As discussed in Lindegren et al. (2016), uncertainties in the final TGAS catalogue are designed to be conservative, and have been 'inflated' from the formal uncertainties derived internally. This was
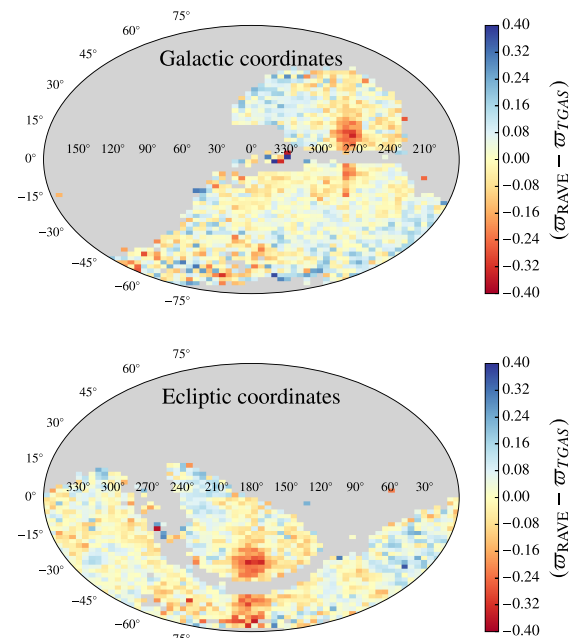

Figure 13. Absolute difference between TGAS parallaxes and the new RAVE-only parallax estimates averaged (median) in bins on the sky in an Aitoff projection, shown in Galactic coordinates (l, b, upper) and ecliptic coordinates (λ, β, lower – note that we have placed $\lambda = 180°$ at the centre of this plot to clearly show the feature). In each plot the grey area is where there are few or no stars. The clearest feature is the patch near $l \sim 280°$, $b \sim 0°$ where TGAS parallaxes appear to be systematically larger than those from RAVE. When looked at in ecliptic coordinates this area can be seen to run from ecliptic pole to ecliptic pole, and is therefore likely to be related to *Gaia*'s scanning law (Arenou et al. 2017).

to take account of uncertainties that are not allowed for in the formal calculation (such as contributions from uncertainties in *Gaia*'s calibration and attitude). The scheme used was derived from a comparison to the (independent) *Hipparcos* parallaxes, and the quoted uncertainties were determined from the formal uncertainties using the formula

$$\sigma_{\varpi,\mathrm{TGAS}}^2 = a^2 \varsigma_{\varpi,\mathrm{TGAS}}^2 + b^2, \tag{24}$$

where $\varsigma_{\varpi,\mathrm{TGAS}}$ is the formal parallax error derived internally, $a = 1.4$ and $b = 0.2$ mas.
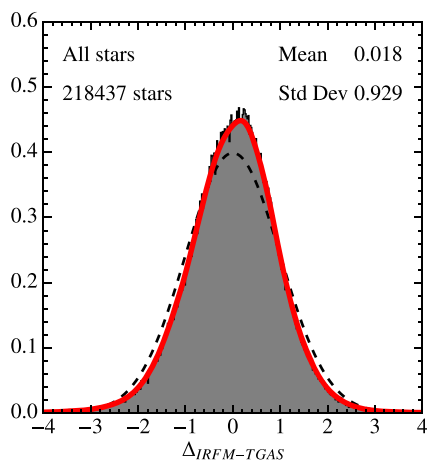
Figure 14. Distribution of Δ for all stars using the new RAVE-only parallax estimates compared to TGAS. The standard deviation is less than unity, implying that the uncertainties of at least one of the parallax estimates have been overestimated.

Gould et al. (2016) looked at the reported parallaxes of RR Lyrae stars in TGAS, and used the known period–luminosity relationship for these stars to provide an independent estimate of the uncertainties in parallax. They found that for these sources $a = 1.1$, $b = 0.12$ mas provides a better description of the true TGAS uncertainties, and therefore recommended that the TGAS parallax estimates should be reduced to a value $\sigma_{\varpi, \text{TGAS, sc}}$ given by the formula

$$\sigma^2_{\varpi, \text{TGAS,sc}} = \alpha^2 \sigma^2_{\varpi, \text{TGAS}} - \beta^2 \quad (25)$$

with $\alpha = 0.79$ and $\beta = 0.10$. They investigated this by looking at how the sum of values of (their equivalent to) Δ^2 varied as they increased the number of values that they summed over (ordered by nominal parallax uncertainty). This was done in the expectation that it should increase linearly with slope unity. For ease of plotting we consider the closely related statistic

$$\chi^2_{\text{red,n}} = \frac{1}{n} \sum_i^n \Delta_i^2, \quad (26)$$

where the sum is over the n sources with the lowest quoted TGAS uncertainty. This should have a constant value of unity as we sum over increasing numbers of sources.

In Fig. 16 we show that, if we use the quoted uncertainties for both RAVE and TGAS, χ^2_{red} remains smaller than unity for all stars. If we use the prescription from Gould et al. (2016) then we come closer to unity when we consider all stars, but χ^2_{red} is clearly less than unity where the sum is over the stars with lower $\sigma_{\varpi, \text{TGAS}}$. This suggests that the Gould et al., prescription gives uncertainties that are still overestimated for stars with small $\sigma_{\varpi, \text{TGAS}}$ and underestimated for those with large $\sigma_{\varpi, \text{TGAS}}$.

Fig. 16 also shows two alternative scenarios. We show χ^2_{red} corresponding to the best values of α and β (assuming that the RAVE uncertainties are correct), which are $\alpha = 0.95$ and $\beta = 0.20$, which corresponds to $b = 0$. Even when we do this (i.e. set the minimum uncertainty from TGAS to zero), the combined uncertainty for the stars with the lowest TGAS uncertainties is clearly too large. We therefore also consider the effect of arbitrarily reducing the RAVE uncertainties according to the formula

$$\sigma_{\varpi, \text{RAVE,sc}} = \gamma \, \sigma_{\varpi, \text{RAVE}}, \quad (27)$$

and find that a value of $\gamma = 0.86$ (while keeping the quoted TGAS uncertainties) produces results that are roughly as good as the results we find when deflating the TGAS uncertainties. It is worth noting that, like the TGAS uncertainties, the RAVE stellar parameter uncertainties were designed to be conservative (Kunder et al. 2017).

It is possible that the RAVE uncertainties tend to be overstated, particularly if the quoted external uncertainty estimates are overstated for most stars. While it certainly would not produce a systematic overestimate that was well described by equation (27), it could affect our estimates in a more complicated and subtle way. We are therefore not in a position to determine for sure whether it is the RAVE uncertainties or TGAS uncertainties (or both) that are overestimated. We would note that a comparison of DR5's parallax estimates to those from *Hipparcos* did not suggest underestimated uncertainties in either instance (Kunder et al. 2017, fig. 25). We add that the dispersion in Δ is smaller than unity for both giants and dwarfs, considered independently. We conclude that our results are consistent with the TGAS uncertainties being underestimated, though probably not in quite the same way as the prescription of Gould et al. (2016). We will not attempt to correct for any overestimates of uncertainty when calculating the combined RAVE+TGAS estimates below.

7 COMBINED DISTANCE ESTIMATES

A fundamental element of Bayesian analysis is the updating of the probability of a hypothesis (for example, the hypothesized distance to a star) as more evidence becomes available. TGAS parallaxes provide new evidence regarding these distances, so we are required to take it into account when determining the distances. We can think of this as either an additional piece of input data, or as a prior on parallax for each star (in addition to the prior on distance implied by equation 13) – the two statements are equivalent.

In previous sections we have investigated the properties of the RAVE distance pipeline in the absence of TGAS parallaxes, and developed an understanding of the problems with each data set. We now incorporate the new evidence from these parallax measurements to obtain more accurate distance estimates than either can provide in isolation. We do this by including them in the set of inputs (O_i, σ_i) in equation (3). It can be expected that the impact of the TGAS parallaxes will be greatest at T_{eff} values below the turn-off where there is serious ambiguity whether a star is on the main sequence or ascending the giant branch – an uncertainty which is reflected in the bimodal pdfs which we are forced to represent using multi-Gaussian fits (equation 4).

We have seen that the parallax estimates (from RAVE alone) for stars with $\log g$ values less than ∼2.0 appear to be particularly biased in the sense that they are systematically lower than those found by TGAS. It is very likely that this is due to the RAVE $\log g$ values in this range being systematically underestimated, as is also suggested by a comparison to the $\log g$ values found by GALAH or APOGEE surveys for the same stars. We noted in Section 4.1 that the TGAS parallax uncertainties for these stars are significantly larger than those found from the RAVE distance pipeline. Therefore, we cannot expect that our distance estimates for these stars are significantly de-biased by including the TGAS parallax in the estimate.

In Fig. 17 we show the average value of Δ (again as a function of $T_{\text{eff, IRFM}}$ for dwarfs and $\log g_{\text{DR5}}$ for giants) for the combined parallax estimates, with the RAVE-only distance estimates (also using the IRFM temperatures) shown for comparison. One must be very careful not to overinterpret these plots for several reasons (e.g.
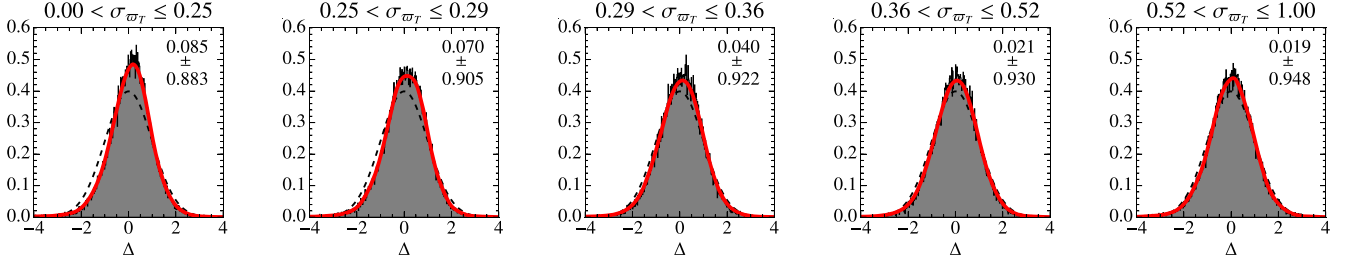
Figure 15. Distribution of Δ using the new RAVE-only parallax estimates, separated into bins by TGAS parallaxes ϖ_T. The standard deviation is less than unity in each case, but increases as ϖ_T increases. This could be because the RAVE uncertainties are consistently overestimated, or because the TGAS uncertainties are particularly overestimated for the smallest uncertainties.
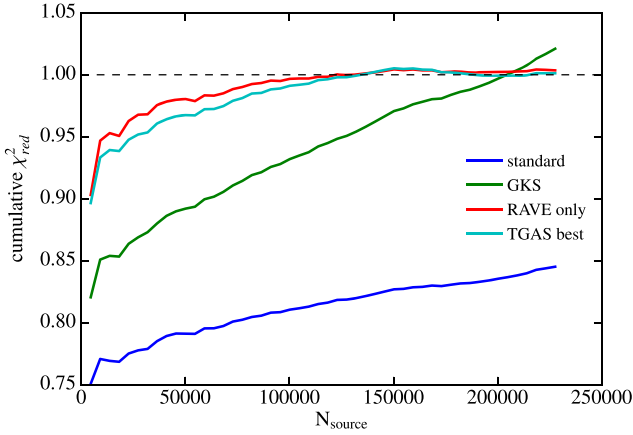

Figure 16. The cumulative reduced χ^2 of the TGAS parallax measurements with the new RAVE-only parallax estimates (equation 26) when the uncertainties of one set or the other have revised downwards. The different lines correspond to the original values (dark blue), the correction from Gould, Kollmeier & Sesar (2016, green; $\alpha = 0.79$ and $\beta = 0.10$ in equation 25), the best correction available when only 'deflating' RAVE uncertainties (red; $\gamma = 0.86$ in equation 27), and the best available only adjusting TGAS uncertainties (light blue; $\alpha = 0.95$ and $\beta = 0.20$)

the RAVE+TGAS parallaxes are obviously not independent of the TGAS ones; the uncertainties for RAVE+TGAS, which enter the calculation of Δ, are generally much smaller than those of RAVE alone), but they clearly indicate that the difference at low $\log g$ values is not removed when we include the TGAS parallax information.

7.1 Improvement

Including the TGAS parallaxes in our distance estimation inevitably leads to an improvement in the formal uncertainties. From the discussion of the previous sections, we can claim with some confidence that, outside a few regions of parameter space (e.g. low $\log g$, the stripe near the ecliptic pole), the combination does not introduce significant systematic errors into one data set or the other.

We can make a naïve estimate of how the uncertainties will decrease when we combine the two data sets by approximating that the uncertainties from the RAVE-only distance pipeline ($\sigma_{\varpi,\mathrm{Sp}}$) are Gaussian, in which case we have a new expected uncertainty in parallax $\sigma_{\varpi,\mathrm{exp}}$ given by

$$1/\sigma_{\varpi,\mathrm{exp}}^2 = 1/\sigma_{\varpi,\mathrm{Sp}}^2 + 1/\sigma_{\varpi,\mathrm{TGAS}}^2. \qquad (28)$$

Because the RAVE uncertainties are significantly non-Gaussian, we do significantly better than this in some regions of the HR diagram.

This can be seen in Fig. 18, which shows the parallax uncertainty we find divided by that which we would naively expect. This is also reflected in the reduced number of stars for which the multi-Gaussian representations are required to describe the distance pdf (lower panel of Fig. 18).

In Fig. 19 we show how the fractional distance uncertainty varies over the HR diagram, both with and without TGAS parallaxes. It is clear that the main improvement is for dwarfs, and for stars in the regions of the HR diagram where parallax information can break uncertainties regarding whether a star is a giant or a dwarf.

When we include TGAS parallaxes, the median fractional distance uncertainty (excluding stars with $\log g_{\mathrm{DR5}} < 2.0$) falls to 15 per cent, from 31 per cent using spectrophotometric information alone. For dwarfs the median uncertainty is just 10 per cent, while for giants it is 19 per cent. The full pdfs of fractional distance uncertainty are shown in Fig. 20.

The improvement over TGAS alone is shown in terms of parallax uncertainty in Fig. 21. In this case it is the giants for which the greatest improvement is found (again excluding stars with $\log g_{\mathrm{DR5}} < 2.0$). The median TGAS uncertainty is 0.32 mas for either giants or dwarfs, while the median uncertainty for RAVE+TGAS is 0.20 mas for giants and 0.24 mas for dwarfs.

Using our combined estimates and the TGAS proper motions, we can convert this distance uncertainty into a velocity uncertainty. We take a simple Monte Carlo approach to do this – for each star we sample from the multi-Gaussian pdf in distance modulus, and from Gaussians in proper motion and radial velocity with the quoted uncertainties. We again assume that the Sun is 8.33 kpc from the Galactic Centre and 15 pc from the Galactic plane. If we characterize the resulting pdf in terms of a median value and a standard deviation (i.e. uncertainty) in each Galactocentric velocity component, we get the distribution of uncertainties shown in Fig. 22. The introduction of TGAS parallaxes to our distance estimates improves the velocity accuracy by, on average, ~40 per cent in each direction.

Finally, we would like to estimate how we could correct our distance estimates to be unbiased. Since we do not know the true values we will do this under the assumption that the TGAS values are unbiased. We make the further approximation that – at a given T_{eff} value for dwarfs or $\log g$ value for giants – we can simply multiply all our RAVE+TGAS parallaxes by a correction factor corr_ϖ such that they are unbiased. For values of $\mathrm{corr}_\varpi \approx 1$ it follows that the equivalent factor for distances is $\mathrm{corr}_s \approx 2 - \mathrm{corr}_\varpi$. We find the value of corr_ϖ by requiring that our statistic $\langle\Delta\rangle$ is zero if we compare $\mathrm{corr}_\varpi \varpi_{\mathrm{RAVE}+\mathrm{TGAS}}$ and ϖ_{TGAS}.

Fig. 23 shows the value of corr_ϖ we find as a function of T_{eff} value for dwarfs and $\log g$ for giants. The dwarfs require systematic
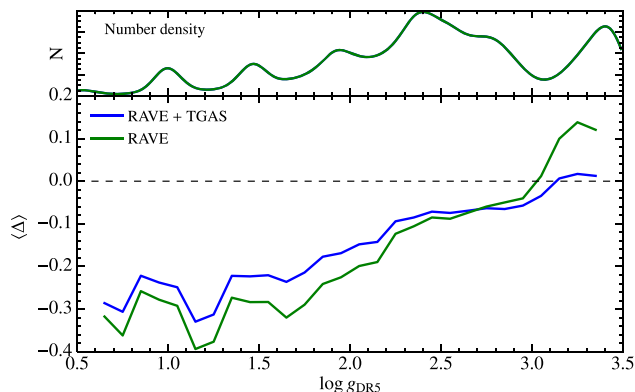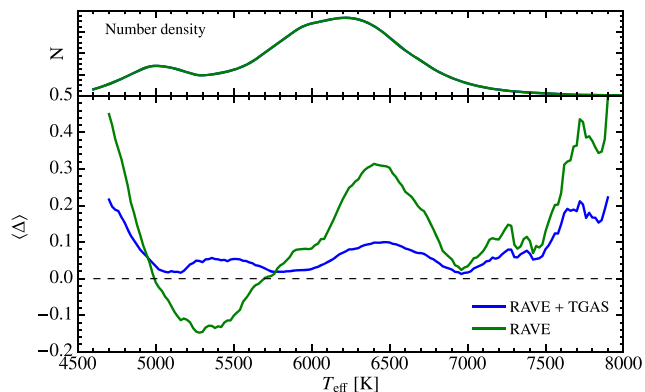
Figure 17. The variation of the average value of Δ (equation 17) as a function of $T_{\rm eff}$ for dwarfs ($\log g \geq 3.5$, left) and as a function of $\log g$ for giants ($\log g < 3.5$, right). The $T_{\rm eff}$ values come from the IRFM. In blue and labelled RAVE+TGAS we show our combined parallax estimates – we also show the RAVE-only estimates (using IRFM $T_{\rm eff}$ values, in green and labelled RAVE, and as shown in Figs 5 and 6) to guide the eye. For low $\log g$ giants, TGAS parallax uncertainties are too large to have a significant effect on the bias seen in RAVE.
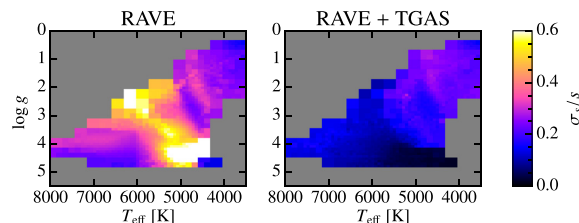

Figure 19. Average fractional distance uncertainties across the HR diagram when we ignore TGAS (left) and when we use the TGAS parallax information (right). The improvement is particularly dramatic for cooler dwarfs and stars with $T_{\rm eff} \sim 6000$ K, $\log g \sim 2.5$. The $T_{\rm eff}$ values come from the IRFM. For low $\log g$ giants, the inclusion of TGAS parallaxes has little effect.

Figure 18. The top panel shows the variation over the HR diagram of the ratio of the actually quoted uncertainty on the parallax when combining TGAS and RAVE data and the expected parallax uncertainty (equation 28) assuming Gaussian uncertainties. The $T_{\rm eff}$ values come from the IRFM. In the region between the dwarf and giant branches and in the red clump the improvement on naive expectations is particularly clear. The lower panels provide an explanation: they show the number of Gaussian components required to represent the pdf in distance modulus (equation 4) without TGAS parallaxes (left) and with them (right). Without the TGAS parallaxes we require a multi-Gaussian representation in $\sim$45 per cent of cases, whereas with TGAS we only need it in $\sim$23 per cent of cases.
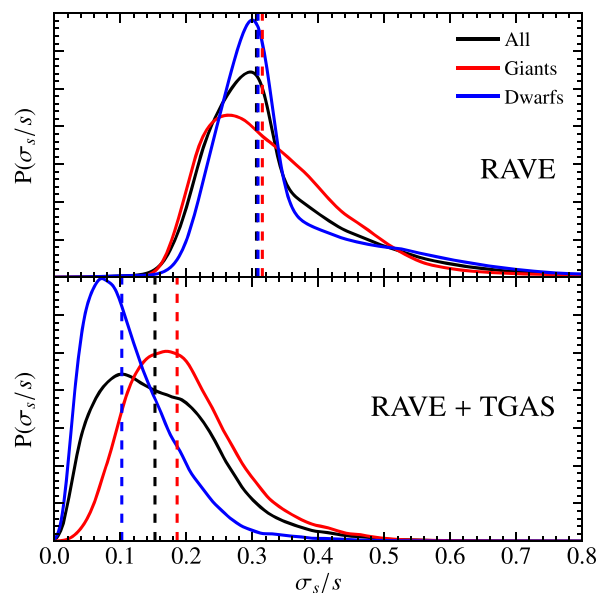

Figure 20. Fractional distance uncertainties for sources when we ignore TGAS parallaxes (upper panel) and when we use TGAS parallaxes (lower panel). In each case we show the pdfs for all sources (black), and separate ones for giants ($2.0 < \log g < 3.5$, red) and dwarfs ($\log g \geq 3.5$, blue). The dashed lines show the median values in each case (0.33 and 0.16 without TGAS and with TGAS, respectively) for all stars (i.e. 51 per cent smaller with TGAS), and 0.36 and 0.20 for giants (44 per cent smaller), and 0.31 and 0.10 for dwarfs (66 per cent smaller).

changes of less than 1 per cent in parallax (or distance) for all but the hottest stars. The giants seem to require systematic changes of more than 10 per cent in parallax at $\log g < 2.0$, up to around 35 per cent at the lowest $\log g$ values. For these low $\log g$ stars, the approximation $\mathrm{corr}_s \approx 2 - \mathrm{corr}_\varpi$ becomes poor.
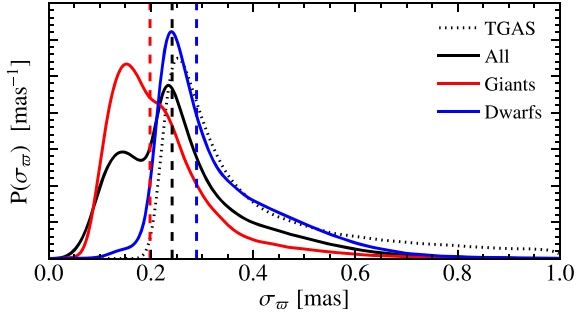
Figure 21. Parallax uncertainties when using the RAVE pipeline with TGAS parallaxes. The dotted curve is the pdf for all stars using just TGAS. The solid lines show the pdfs for all sources (black), and separate ones for giants ($2.0 < \log g < 3.5$, red) and dwarfs ($\log g \geq 3.5$, blue). The dashed lines show the median values in each case which can be compared to the median TGAS uncertainty for these stars, which is 0.32 mas (essentially independently of whether stars are dwarfs or giants). This median is 0.25 mas for all stars (24 per cent smaller than TGAS), 0.15 mas for giants (54 per cent smaller), and 0.29 mas for dwarfs (9 per cent smaller).
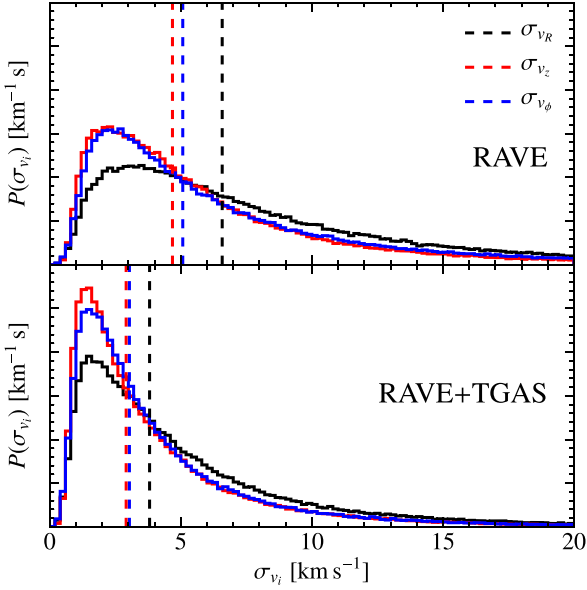

Figure 22. Velocity uncertainties for sources when we ignore TGAS parallaxes (upper panel) and when we use TGAS parallaxes (lower panel). In each case we show the pdfs in v_R (black), v_z (red), and v_φ (blue). The dashed lines show the median values in each case, which are 6.6 and 3.8 km s^{-1} (without TGAS and with TGAS, respectively) for v_R, 4.7 and 2.9 km s^{-1} for v_z, and 5.1 and 3.0 km s^{-1} for v_φ, i.e. the velocity uncertainty in each direction is reduced by $\sim$40 per cent.

8 AGE ESTIMATES

The classical method for determining the age of a star is by comparing the luminosity of an F or G star to that expected for stars of its colour on the main sequence or turning off it. This is only possible if an independent estimate of its distance (e.g. a parallax) is available. By including TGAS parallaxes in the RAVE pipeline we are making precisely this comparison, with additional information and a sophisticated statistical treatment. We can therefore expect that the ages we derive are as reliable as any currently available for main-sequence stars.
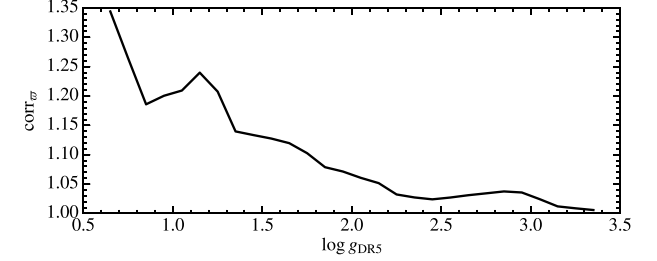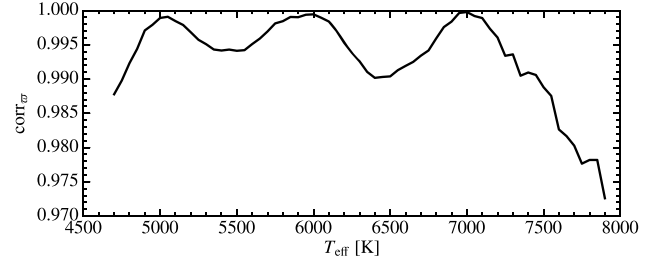

Figure 23. Estimated parallax correction factors (corr$_\varpi$) for the RAVE+TGAS combined parallax estimates as a function of T_{eff} for dwarfs ($\log g \geq 3.5$, upper) and $\log g$ for giants ($\log g < 3.5$, lower). Values are calculated in as a running average over a window of width 200 K or 0.3 dex. If we multiply all the RAVE+TGAS ϖ values in this window by corr$_\varpi$, then Δ is, on average, zero.

While the original aim of this pipeline was to determine the distances to stars, an inevitable by-product is that we also constrain the other 'model' properties described in Section 2, i.e. initial mass $\mathcal{M}$, age τ, metallicity [M/H], and line-of-sight extinction A_V. We can also produce new estimates of the other properties of the stars, such as T_{eff} and $\log g$, which we discuss below.

Here, we look at the improved estimates of τ that are made possible by including TGAS parallaxes. Age estimates from this pipeline were included in RAVE DR4 (in terms of $\log \tau$), but came with the strong caveat that the prior used (the Standard prior; see our Section 2.1) included a fixed relationship between metallicity and age (metal-poor stars are assumed to be old, metal-rich stars younger). In our case, we have now seen that we can use a prior without any explicit age–metallicity relationship and still produce reasonable results (at least in terms of parallaxes – Fig. 12). This gives us some confidence that we will not go too badly wrong using this prior when deriving ages.

We would expect that the addition of the TGAS parallax measurements provides us with substantial leverage when determining the ages of stars, and in Fig. 24 we quantify this. It is clear that, particularly at the low-uncertainty end, we do have a substantial improvement in precision. Without TGAS only 1.5 per cent of stars have fractional age uncertainties lower than 0.3, while with TGAS this increases to over 25 per cent. In Fig. 25 we show where in the HR diagram the stars with the smallest age uncertainties are found. As one would expect, they are primarily found near the main-sequence turn-off – it is in this region that stars evolve quickly with age, and it is therefore possible to get an age estimate with small uncertainties even with imperfect observations.

It is clear from Fig. 17 that there are still some biases in the distance estimates for dwarfs with $6000 \lesssim T_{\text{eff}} \lesssim 7000$ K (i.e. in the main-sequence turn-off region), though Fig. 23 suggests that these are only at the 1 per cent level. It is reasonable to ask whether this implies a bias in the age estimates. We cannot know for sure,
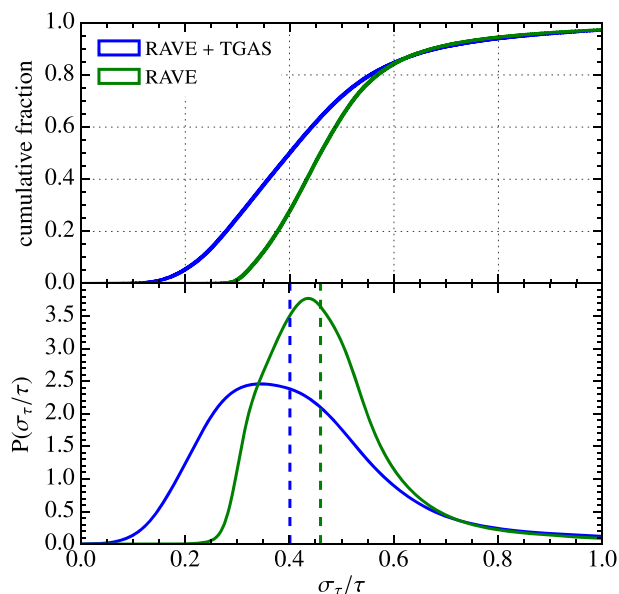
Figure 24. The fraction of sources with a given fractional age uncertainty (σ_τ/τ) displayed as a pdf found using a kernel density estimation (lower panel), and as a cumulative distribution (upper panel). The median values are plotted as dashed lines. The plot shows the distribution of age uncertainties with and without TGAS parallaxes (blue and green curves, respectively). It is particularly clear that the inclusion of TGAS parallaxes allows us to derive age uncertainties of less than 30 per cent for a significant fraction of sources.

provement over past studies (Wojno et al. 2016) in understanding the relationship between age, metallicity, and velocity of stars in the Solar neighbourhood which is made possible by the TGAS parallaxes.

9 STELLAR PARAMETERS

The Bayesian pipeline takes $\log g$ and T_{eff} as inputs to the likelihood calculation, taken either directly from the spectroscopic pipeline or from the IRFM. It also inevitably (if usually implicitly) determines a posterior probability distribution for these parameters. The increased information that we now have about the stars (primarily from TGAS) means that these posterior probability distributions are significantly better estimates of the stellar parameters than those we input. In future these may be used to provide estimates for use in the pipeline that determines the chemical abundances, and may be used without giving any input from the spectroscopic pipeline other than metallicity. Because the intention is to provide estimates of these stellar parameters, rather than take them as input, we refer to this as the *reverse pipeline*, though it is fundamentally the same machinery. The use of parallaxes to improve estimates of $\log g$ is far from new (e.g. Bensby, Feltzing & Lundström 2003), and here we simply extend it in much the same way as is being planned within the *Gaia* consortium (e.g. Bailer-Jones et al. 2013).

Fig. 26 shows the HR diagram using the best estimates of T_{eff} and $\log g$ from the Bayesian pipeline (referred to as $T_{\text{eff, PJM}}$, $\log g_{\text{PJM}}$). We show the density of stars in this plane using a contour (showing a strong red clump) and colour regions of the diagram by the median metallicity of stars in that region. This can cause artefacts in regions with few stars, such as above the main sequence. It is worth noting that the sources with $\log g_{DR5} < 2$ do not have their $\log g$ values significantly shifted. This is because the TGAS parallaxes are too uncertain to have much of an effect (see Fig. 7). Future *Gaia* data releases will have smaller parallax uncertainties, so this approach is a viable one to improve the $\log g$ values for these stars after *Gaia* DR2, on 2018 April 25.

We caution that the stars found in regions of the HR diagram away from typical isochrones (e.g. above the main sequence) are likely to have rather untrustworthy parameters from our pipeline. This is because our framework is not designed to deal with unusual objects such as binaries (which naturally lie above the main sequence in the colour–magnitude version of the HR diagram). The large majority of these stars are flagged in DR5 using the Matijevič et al. (2012) approach (for example, ~900 of the ~1000 found above the main sequence with $T_{\text{eff, PJM}} < 5500$ K are flagged), and therefore flagged in our catalogue.

The clean appearance of this HR diagram is to a large extent by construction, because stellar models are used to determine a star's place on the diagram. For a true test of the reliability of this method we must look at comparisons to external catalogues.

Kunder & RAVE Collaboration (2017) were the first to highlight the decrease in scatter in the T_{eff} and $\log g$ values from the reverse pipeline as compared to the RAVE pipeline alone. Figs 27, 28, and 29 show a more detailed comparison in the T_{eff} and $\log g$ parameters from RAVE DR5, RAVE-on (found from the RAVE spectra using a data-driven approach by Casey et al. 2017) and those presented here compared to high-resolution spectroscopy parameters. First, Fig. 27 shows the 67 stars presented here that could be matched with high-resolution field star studies from Schlaufman & Casey (2014), Ishigaki, Aoki & Chiba (2013), and Roederer et al. (2014), from open and globular clusters Blanco 1 (Ford, Jeffries & Smalley 2005), 47 Tuc (Koch & McWilliam 2008; Carretta et al. 2009;
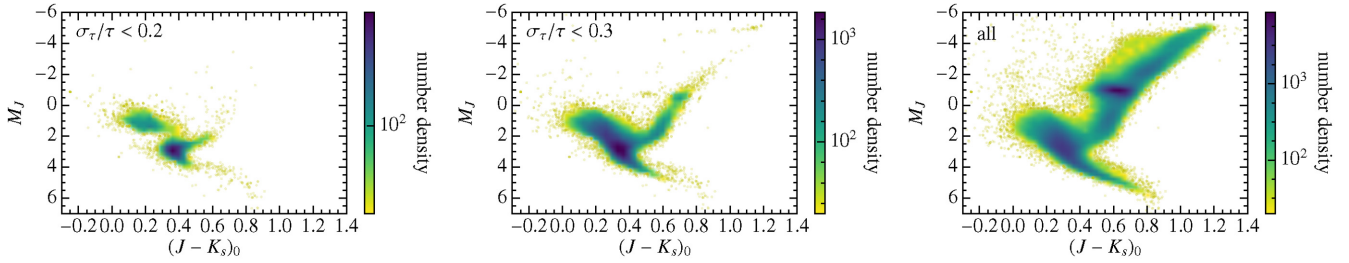
because we do not know what causes the bias. We have investigated the possible biases by running the pipeline having either artificially decreased the input $\log g$ values by 0.4 dex or artificially decreased the input parallaxes by 50 µas. Either change results in parallax estimates that are biased in the opposite sense to that seen with the real data for these stars. In both cases the changes in stellar ages are small compared to the uncertainties. The change in input $\log g$ produces a typical change of ~0.5 Gyr (or 5–10 per cent) but with no trend to higher or lower ages (i.e. no clear bias). The change in input ϖ produces a smaller typical change of ~0.2 Gyr (or ~4 per cent) with a bias in the sense that cooler stars (with $T_{\text{eff}} \sim 6000$) have slightly lower ages than those originally quoted, by ~0.1 Gyr (or ~2 per cent). These are negligible for most purposes, but it is entirely possible that other biases in the analysis (for example in the metallicities or the stellar isochrones) have larger impacts on the age estimates. The study of the complex interplay of these different factors is beyond the scope of this paper.

We must caution that these age estimates are extremely hard to verify from external sources. A relatively small number of sources have age estimates from asteroseismology studies or because they are part of clusters with known ages, and these are sources for which we have large age uncertainties. We can gain confidence from the facts that (1) the method we are using to determine distances and ages has been carefully tested with pseudo-data for accuracy by, amongst others, Burnett & Binney (2010); and (2) the application of this method to these data to find distances has been rigorously tested against TGAS parallaxes in this study, and we have found that it is generally successful (except for $\log g < 2.0$ stars, where we believe that the problem lies in the quoted $\log g$ values).

In a forthcoming paper (Wojno et al. 2018) we will use these age estimates to isolate young and old populations in the RAVE catalogue and study their properties. This will demonstrate the im-

Figure 25. The location of stars with small fractional age uncertainties in the HR diagram (with colour and absolute magnitude on the two axes in this case). Both the $(J - K_s)$ colour and the absolute magnitude in the J band, M_J, have been corrected for extinction using the most likely $\log A_V$ value found by the distance pipeline. The left figure shows those with age uncertainties less than 20 per cent, the central figure those with age uncertainties less than 30 per cent, and the right figure shows all stars (for comparison). The number density indicated by the colour bar corresponds to the numbers of stars in a pixel of height 0.1 mag in M_J and width 0.01 mag in $(J - K_s)_0$. Unsurprisingly, the smallest fractional age uncertainties are for stars near the main-sequence turn-off.
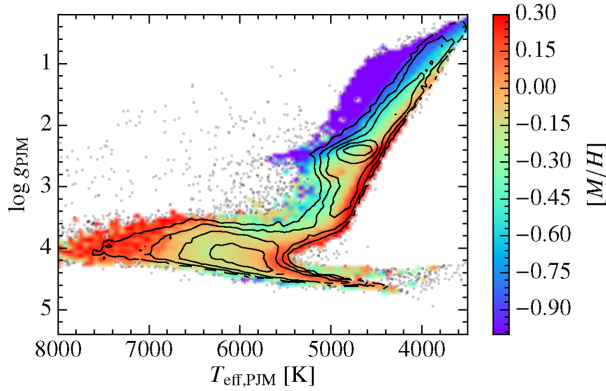

Figure 26. Output from the 'reverse pipeline', which finds the $T_{\rm eff}$ and $\log g$ values of the stars using the Bayesian method described in this paper. Pixels are coloured by median metallicity, and overlaid contours show the density (with a logarithmic scaling in density between contours).
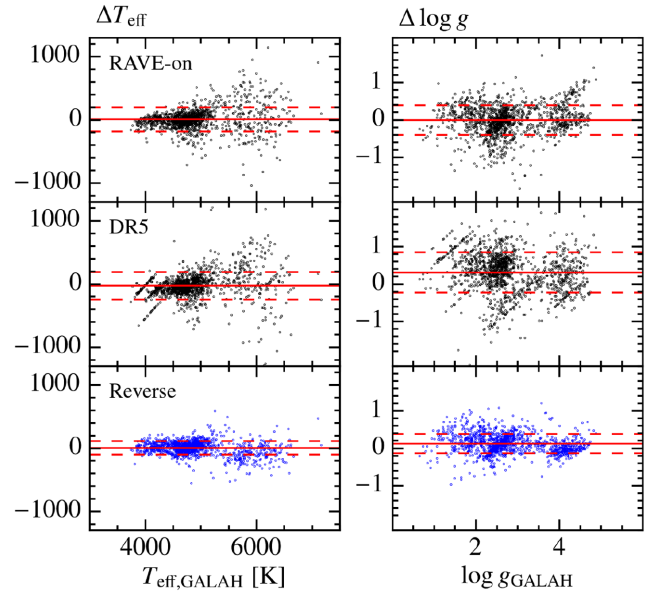

Figure 27. Comparison of parameters from RAVE-on, DR5, and the reverse pipeline to those from high-resolution field stars studies (as described in the text). Note that the y-axis labels are placed at the top of the figure (i.e. $\Delta T_{\rm eff}$, $\Delta \log g$). The differences are given in the sense, e.g. $\log g_{\rm DR5} - \log g_{\rm ext}$. The solid red lines indicate the mean values; the dashed red lines are placed one standard deviation either side. In each case the reverse pipeline parameters show less bias and less spread.
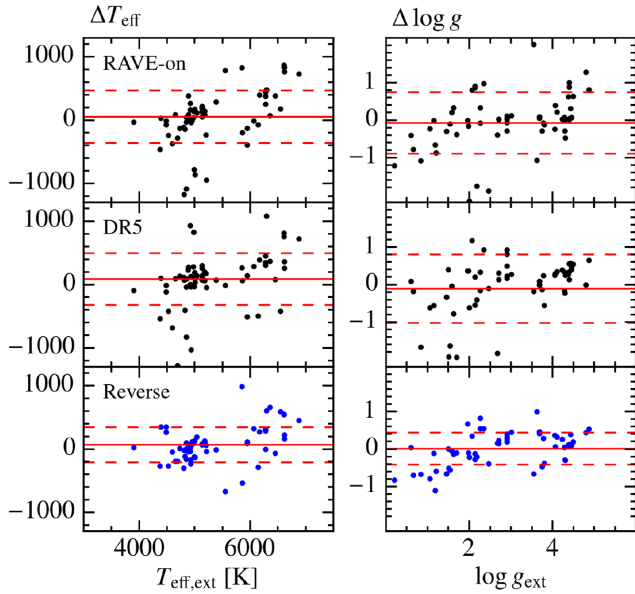

Figure 28. As Fig. 27, except it uses parameters from GALAH for the comparison to parameters from RAVE-on, DR5, and the reverse pipeline. Again the spread of values from the reverse pipeline is far smaller than in either other case.
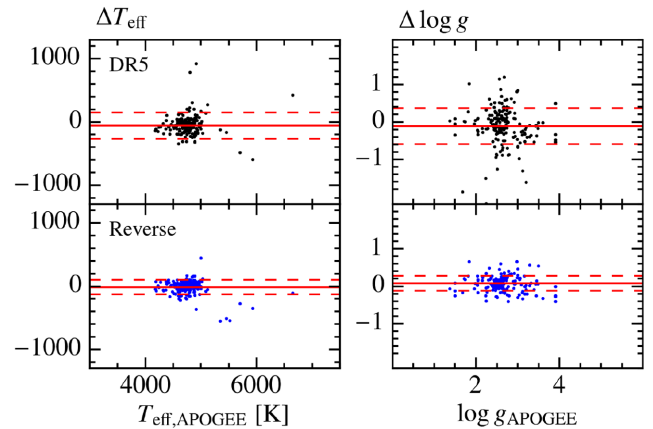

Figure 29. As Figs 27 and 28, except it uses parameters from APOGEE for the comparison to parameters from DR5, and the reverse pipeline. We do not compare RAVE-on with APOGEE, as RAVE-on uses the RAVE–APOGEE overlap stars as part of their training sample. Again, we find that the scatter and bias are substantially reduced.

Cordero et al. 2014), Pleiades (Funayama et al. 2009), NGC 2632 (Yang, Chen & Zhao 2015), and IC 4651 (Carretta et al. 2004; Pasquini et al. 2004), as well as from the *Gaia*-ESO survey (Gilmore et al. 2012).

The difference in log g between these studies and those presented here is 0.0 ± 0.42 dex, as compared to -0.08 ± 0.83 and -0.11 ± 0.92 dex from RAVE-on and RAVE DR5, respectively. Upon selecting the 53 stars with an SNR >40, the difference in log g is reduced to 0.03 ± 0.38 dex, as compared to -0.06 ± 0.72 and 0.00 ± 0.83 dex from RAVE-on and RAVE DR5, respectively.

The scatter in T_{eff} is also improved when adopting the temperatures presented here. The difference in T_{eff} between the high-resolution studies and those presented here is 75 ± 282 K as compared to 51 ± 420 K and 86 ± 410 K from RAVE-on and RAVE DR5, respectively. Using the stars with an SNR >40, the difference in T_{eff} is 81 ± 262 K as compared to 45 ± 372 K and 87 ± 390 K from RAVE-on and RAVE DR5, respectively.

Fig. 28 shows how the T_{eff} and log g parameters from RAVE DR5, RAVE-on, and those presented here compare to those from GALAH DR1, a high-resolution ($R \sim 28\,000$) spectroscopic survey. From 1379 overlap stars, the difference between GALAH log g and that presented here is 0.12 ± 0.26 dex, compared to 0.0 ± 0.40 dex from RAVE-on and 0.3 ± 0.54 dex from RAVE DR5. From the 753 overlap stars with the best RAVE stellar parameters (i.e. AlgoConv $=0$ and SNR >40), the difference between GALAH log g and that presented here is 0.11 ± 0.22 dex, compared to -0.03 ± 0.33 dex from RAVE-on and 0.37 ± 0.42 dex from RAVE DR5.

Lastly, we present a comparison of the stellar parameters presented here to APOGEE ($R \sim 22\,500$, Fig. 29). Note that we do not compare RAVE-on with APOGEE, as RAVE-on uses the RAVE–APOGEE overlap stars as part of their training sample. From 183 overlap stars, we find the difference between APOGEE log g and that presented here is 0.07 ± 0.20 dex, compared to -0.11 ± 0.49 dex from RAVE DR5. The difference between APOGEE T_{eff} and that presented here is -24 ± 124 K, compared to -58 ± 210 K from RAVE DR5. The 146 overlap stars with AlgoConv $=0$ and SNR >40 have a difference in log g between APOGEE and that presented here of 0.08 ± 0.19 dex, compared to -0.06 ± 0.39 dex from RAVE DR5. The difference between APOGEE T_{eff} and that presented here is -23 ± 101 K, compared to -69 ± 116 K from RAVE DR5.

Therefore, from a variety of different high-resolution studies, we conclude that the scatter in log g is a factor of 2 smaller when using surface gravities from the reverse pipeline as compared to both RAVE-on and RAVE DR5 parameters. Also, for stars with a low SNR (<40), the gravities and temperatures from the reverse pipeline are reliable, equal to or even better than the gravities and temperatures determined from the high-SNR stars in RAVE DR5 and RAVE-on.

It is our plan to use this method in an iterative fashion with the RAVE spectroscopic pipeline to improve the accuracy of our stellar parameters and therefore the RAVE abundance estimates. We anticipate that the results will be released as part of RAVE DR6.

10 CONCLUSIONS

We have produced new distance, age, and stellar parameter estimates for stars common to RAVE and TGAS which reflect new measurements of parallax and T_{eff} (from TGAS and the IRFM, respectively). This allows us to produce distance estimates that are better than those that either RAVE or TGAS can achieve in isola-

Table 3. Data flags specific to this study. In all cases 1 indicates a potential problem with the distance estimate.

Name	Explanation
flag_low_logg	log $g_{\mathrm{DR5}} < 2.0$ (see Section 4.1).
flag_outlier	TGAS and RAVE-only parallaxes differ by more than 4σ – RAVE not used for final distances (see Section 4.2).
flag_N	Spectrum flagged as not normal by Matijevič et al. (2012).
flag_pole	Source lies in the problematic region near the ecliptic pole ($165° < \lambda < 195°$, $\beta < -30°$; see Section 6).
flag_dup	A spectrum of the same star with a higher SNR is in RAVE.
flag_any	True if any of the above are true, otherwise false.

tion. It also allows us to make age estimates which have better than 30 per cent precision for 25 per cent of the stars in our sample, and estimates of the stellar parameters which are roughly twice as accurate as from RAVE spectra alone (when compared to external catalogues).

RAVE is the spectroscopic survey with the largest number of sources in common with TGAS, and therefore this data set has the largest number of sources with both radial velocities from spectroscopy and proper motions from space astrometry. The improvement in distance uncertainty due to this study provides a substantial decrease in the uncertainty on the 3D velocities of these stars. When combined with our age estimates, this gives new insight into the history of our Galaxy.

We have carefully tested the RAVE distance pipeline and the TGAS parallaxes against one another. From this comparison we can draw several conclusions:

(i) The RAVE DR5 parallaxes were overestimated for dwarfs with $T_{\mathrm{eff}} \gtrsim 5500$ K and underestimated for giants with log $g \lesssim 2.0$ dex. This corresponds to a T_{eff} underestimate in the former case, and a log g underestimate in the latter. We can (mostly) correct for the former by using the IRFM temperatures provided with DR5, but correcting for the latter is beyond the scope of this study.

(ii) When we use the IRFM T_{eff} values to find spectrophotometric parallaxes, the two parallax estimates agree well in the vast majority of cases, with systematic differences that are substantially smaller than the statistical ones.

(iii) A comparison as a function of position on the sky indicates that the TGAS parallaxes appear to be overestimated by ~ 0.3 mas in a region of the sky near Galactic coordinates $(l, b) = (100°, 0°)$ which is also near the ecliptic pole (see also Arenou et al. 2017; Schönrich & Aumer 2017).

(iv) The small random differences between the RAVE-only parallax estimates and the TGAS parallaxes, and the fact that this is found for many stellar types, suggest that the TGAS random uncertainties are overestimated by ~ 0.2 mas.

We provide flags with our distance estimates, as indicated in Table 3. To use a 'clean' set of stars we recommend that users take only stars with the flag 'flag_all$=0$'. This yields a set of 137 699 stars.

As with previous distance estimates from RAVE, we characterize the output pdf from our distance pipeline by the expectation value and uncertainty in distance, distance modulus, and parallax, and by a multi-Gaussian pdf in distance modulus. This last option provides the most complete description of what the distance pipeline finds, though it is clearly less important here than it was before TGAS parallaxes became available (Fig. 18).

Table 4. Catalogue description. Entries labelled [1] are derived in this study. Entries labelled [2] are used to derive the values found in this study. Entries labelled [3] were derived for RAVE DR5, and further explanation can be found in Kunder et al. ([2017]).

Col	Units	Name	Explanations
1	–	RAVE_OBS_ID	Target designation [3]
2	–	RAVEID	RAVE target designation [3]
3	deg	RAdeg	Right ascension [2][3]
4	deg	DEdeg	Declination [2][3]
5	deg	Glon	Galactic longitude [3]
6	deg	Glat	Galactic latitude [3]
7	$\mathrm{km\,s^{-1}}$	HRV	Heliocentric radial velocity [3]
8	$\mathrm{km\,s^{-1}}$	eHRV	HRV error [3]
9	$\mathrm{mas\,yr^{-1}}$	pmRA_TGAS	Proper motion in RA from TGAS ($\dot{\alpha}\cos\delta$)
10	$\mathrm{mas\,yr^{-1}}$	pmRA_error_TGAS	Standard uncertainty in proper motion in RA from TGAS
11	$\mathrm{mas\,yr^{-1}}$	pmDE_TGAS	Proper motion in DE from TGAS (δ)
12	$\mathrm{mas\,yr^{-1}}$	pmDE_error_TGAS	Standard uncertainty in proper motion in DE from TGAS
13	pc	distance	Distance estimate [1]
14	pc	distance_err	Distance uncertainty [1]
15	yr	age	Stellar age estimate [1]
16	yr	age_err	Stellar age uncertainty [1]
17	$M_\odot$	mass	Stellar mass estimate [1]
18	$M_\odot$	mass_err	Stellar mass uncertainty [1]
19	–	log_A_V	$\log_{10}A_V$ extinction estimate [1]
20	–	log_A_V_err	$\log_{10}A_V$ extinction uncertainty [1]
21	mas	parallax	Parallax estimate [1]
22	mas	parallax_err	Parallax uncertainty estimate [1]
23	–	dist_mod	Distance modulus estimate [1]
24	–	dist_mod_err	Distance modulus uncertainty [1]
25	–	Teff_PJM	T_{eff} estimate [1]
26	–	Teff_PJM_err	T_{eff} uncertainty [1]
27	–	logg_PJM	$\log g$ estimate [1]
28	–	logg_PJM_err	$\log g$ uncertainty [1]
29	–	number_of_Gaussians_fit	Number of components for multi-Gaussian fit (N_{Gau} in equation 4) [1]
30	–	mean_1	Parameter for multi-Gaussian fit ($\widehat{\mu_1}$ in equation 4) [1]
31	–	sig_1	Parameter for multi-Gaussian fit (σ_1 in equation 4) [1]
32	–	frac_1	Parameter for multi-Gaussian fit (f_1 in equation 4) [1]
33	–	mean_2	Parameter for multi-Gaussian fit ($\widehat{\mu_2}$ in equation 4) [1]
34	–	sig_2	Parameter for multi-Gaussian fit (σ_2 in equation 4) [1]
35	–	frac_2	Parameter for multi-Gaussian fit (f_2 in equation 4) [1]
36	–	mean_3	Parameter for multi-Gaussian fit ($\widehat{\mu_3}$ in equation 4) [1]
37	–	sig_3	Parameter for multi-Gaussian fit (σ_3 in equation 4) [1]
38	–	frac_3	Parameter for multi-Gaussian fit (f_3 in equation 4) [1]
39	–	FitQuality_Gauss	Quality of multi-Gaussian fit, as described by equation (5) [1]
40	–	Fit_Flag_Gauss	Quality flag for multi-Gaussian fit, as discussed in Section 2 [1]
41	–	AV_Schlegel	Extinction used in prior ($A_V^{\mathrm{pr}}(\infty, l, b)$ in equation 9) [2]
42	–	logg_N_K	RAVE DR5 Calibrated log gravity [2][3]
43	–	elogg_K	RAVE DR5 Internal uncertainty log gravity [2][3]
44	K	Teff_IR	Temperature from IRFM [2][3]
45	K	eTeff_IR	Internal uncertainty on temperature from IRFM [2][3]
46	dex	Met_N_K	Calibrated metallicity [M/H] [2][3]
47	dex	eMet_K	Internal uncertainty on calibrated metallicity [M/H] [2][3]
48	mas	parallax_TGAS	Parallax from TGAS [2]
49	mas	parallax_error_TGAS	Quoted uncertainty on parallax from TGAS [2]
50	–	Jmag_2MASS	J-magnitude from 2MASS [2]
51	–	eJmag_2MASS	Uncertainty on J-magnitude from 2MASS [2]
52	–	Hmag_2MASS	H-magnitude from 2MASS [2]
53	–	eHmag_2MASS	Uncertainty on H-magnitude from 2MASS [2]
54	–	Kmag_2MASS	K-magnitude from 2MASS [2]
55	–	eKmag_2MASS	Uncertainty on K-magnitude from 2MASS [2]
56	–	W1mag_ALLWISE	$W1$-magnitude from AllWISE [2]
57	–	eW1mag_ALLWISE	Uncertainty on $W1$-magnitude from AllWISE [2]
58	–	W2mag_ALLWISE	$W2$-magnitude from AllWISE [2]
59	–	eW2mag_ALLWISE	Uncertainty on $W2$-magnitude from AllWISE [2]
60	dex	Mg	Abundance of Mg [Mg/H] [3]
61	–	Mg_N	The number of spectral lines used for calculation of abundance [3]
62	dex	Al	Abundance of Al [Al/H] [3]
63	–	Al_N	The number of spectral lines used for calculation of abundance [3]

Table 4. *– continued*

Col	Units	Name	Explanations
64	dex	Si	Abundance of Si [Si/H] [3]
65	–	Si_N	Number of spectral lines used for calculation of abundance [3]
66	dex	Ti	Abundance of Ti [Ti/H] [3]
67	–	Ti_N	The number of spectral lines used for calculation of abundance [3]
68	dex	Fe	Abundance of Fe [Fe/H] [3]
69	–	Fe_N	The number of spectral lines used for calculation of abundance [3]
70	dex	Ni	Abundance of Ni [Ni/H] [3]
71	–	Ni_N	The number of spectral lines used for calculation of abundance [3]
72	–	c1	Spectral flag following Matijevič et al. (2012) [3]
73	–	c2	Spectral flag following Matijevič et al. (2012) [3]
74	–	c3	Spectral flag following Matijevič et al. (2012) [3]
75	–	c4	Spectral flag following Matijevič et al. (2012) [3]
76	–	c5	Spectral flag following Matijevič et al. (2012) [3]
77	–	c6	Spectral flag following Matijevič et al. (2012) [3]
78	–	c7	Spectral flag following Matijevič et al. (2012) [3]
79	–	c8	Spectral flag following Matijevič et al. (2012) [3]
80	–	c9	Spectral flag following Matijevič et al. (2012) [3]
81	–	c10	Spectral flag following Matijevič et al. (2012) [3]
82	–	c11	Spectral flag following Matijevič et al. (2012) [3]
83	–	c12	Spectral flag following Matijevič et al. (2012) [3]
84	–	c13	Spectral flag following Matijevič et al. (2012) [3]
85	–	c14	Spectral flag following Matijevič et al. (2012) [3]
86	–	c15	Spectral flag following Matijevič et al. (2012) [3]
87	–	c16	Spectral flag following Matijevič et al. (2012) [3]
88	–	c17	Spectral flag following Matijevič et al. (2012) [3]
89	–	c18	Spectral flag following Matijevič et al. (2012) [3]
90	–	c19	Spectral flag following Matijevič et al. (2012) [3]
91	–	c20	Spectral flag following Matijevič et al. (2012) [3]
92	–	SNR	Signal-to-noise value [3]
93	–	Algo_Conv_K	Quality flag for stellar parameter pipeline [0..4] [3]
94	–	flag_lowlogg	Quality flag (see Table 3) [1]
95	–	flag_outlier	Quality flag (see Table 3) [1]
96	–	flag_N	Quality flag (see Table 3) [1]
97	–	flag_pole	Quality flag (see Table 3) [1]
98	–	flag_dup	Quality flag (see Table 3) [1]
99	–	flag_any	Quality flag (see Table 3) [1]

The apparatus we have used for this study is applicable to data from any spectroscopic survey. It is our intention to apply it to data from the APOGEE survey in the near future.

We will also produce distance estimates for RAVE stars that do not have TGAS parallaxes, using the AllWISE photometry and IRFM temperatures. These will have smaller systematic errors than the DR5 distances, particularly for hot dwarfs, because of the use of IRFM $T_{\rm eff}$ values. All of these distance estimates will be made available through the RAVE website (http://dx.doi.org/10.17876/rave/dr.5/033 and http://dx.doi.org/10.17876/rave/dr.5/034 for the distance estimates for sources with and without TGAS parallaxes, respectively). For TGAS sources they constitute a substantial improvement in distance and, therefore, velocity uncertainty over previous data releases. It is our hope that the new, more precise age and distance estimates are of great value in characterizing the dynamics and history of our Galaxy.

DPAC has been provided by national institutions, in particular the institutions participating in the *Gaia* Multilateral Agreement.

REFERENCES

Anguiano B. et al., 2015, MNRAS, 451, 1229
Arce H. G., Goodman A. A., 1999, ApJ, 512, L135
Arenou F. et al., 2017, A&A, 599, A50
Astraatmadja T. L., Bailer-Jones C. A. L., 2016, ApJ, 833, 119
Aumer M., Binney J. J., 2009, MNRAS, 397, 1286
Bailer-Jones C. A. L., 2015, PASP, 127, 994
Bailer-Jones C. A. L. et al., 2013, A&A, 559, A74
Barnes T. G., III, Jefferys W. H., Berger J. O., Mueller P. J., Orr K., Rodriguez R., 2003, ApJ, 592, 539
Bensby T., Feltzing S., Lundström I., 2003, A&A, 410, 527
Binney J., Gerhard O., Spergel D., 1997, MNRAS, 288, 365
Binney J. et al., 2014, MNRAS, 437, 351
Blackwell D. E., Shallis M. J., Selby M. J., 1979, MNRAS, 188, 847
Bressan A., Marigo P., Girardi L., Salasnich B., Dal Cero C., Rubele S., Nanni A., 2012, MNRAS, 427, 127
Burnett B., Binney J., 2010, MNRAS, 407, 339
Burnett B. et al., 2011, A&A, 532, A113
Carollo D. et al., 2010, ApJ, 712, 692
Carretta E., Bragaglia A., Gratton R. G., Tosi M., 2004, A&A, 422, 951
Carretta E., Bragaglia A., Gratton R., Lucatello S., 2009, A&A, 505, 139
Casagrande L., Ramírez I., Meléndez J., Bessell M., Asplund M., 2010, A&A, 512, A54
Casey A. R. et al., 2017, ApJ, 840, 59
Chabrier G., 2003, PASP, 115, 763
Cordero M. J., Pilachowski C. A., Johnson C. I., McDonald I., Zijlstra A. A., Simmerer J., 2014, ApJ, 780, 94
Cutri R. M. et al., 2012, Technical Report, Explanatory Supplement to the WISE All-Sky Data Release Products
Cutri R. M. et al., 2013, VizieR Online Data Catalog, 2328
Davies G. R. et al., 2017, A&A, 598, L4
Ford A., Jeffries R. D., Smalley B., 2005, MNRAS, 364, 272
Funayama H., Itoh Y., Oasa Y., Toyota E., Hashimoto O., Mukai T., 2009, PASJ, 61, 931
Gaia Collaboration, 2016a, A&A, 595, A1
Gaia Collaboration, 2016b, A&A, 595, A2
Gillessen S., Eisenhauer F., Trippe S., Alexander T., Genzel R., Martins F., Ott T., 2009, ApJ, 692, 1075
Gilmore G. et al., 2012, The Messenger, 147, 25
Gontcharov G. A., Mosenkov A. V., 2017, MNRAS, 470, L97
Gould A., Kollmeier J. A., Sesar B., 2016, preprint (arXiv:1609.06315)
Haywood M., 2001, MNRAS, 325, 1365
Heiter U., Jofré P., Gustafsson B., Korn A. J., Soubiran C., Thévenin F., 2015, A&A, 582, A49
Helmi A., Veljanoski J., Breddels M. A., Tian H., Sales L. V., 2017, A&A, 598, A58
Howell S. B. et al., 2014, PASP, 126, 398
Hunt J. A. S., Bovy J., Carlberg R. G., 2016, ApJ, 832, L25
Høg E. et al., 2000, A&A, 355, L27
Ishigaki M. N., Aoki W., Chiba M., 2013, ApJ, 771, 67
Jurić M. et al., 2008, ApJ, 673, 864
Jørgensen B. R., Lindegren L., 2005, A&A, 436, 127
Koch A., McWilliam A., 2008, AJ, 135, 1551
Kordopatis G., Recio-Blanco A., de Laverny P., Bijaoui A., Hill V., Gilmore G., Wyse R. F. G., Ordenovic C., 2011, A&A, 535, A106
Kordopatis G. et al., 2013, AJ, 146, 134
Kroupa P., 2001, MNRAS, 322, 231
Kunder A., RAVE Collaboration, 2017, in Recio-Blanco A., de Laverny P., Brown A. G. A., Prusti T., eds, Proc. IAU Symp. 330, Astronomy and Astrophysics in the Gaia Sky. Kluwer, Dordrecht, 176

Kunder A. et al., 2017, AJ, 153, 75
Lindegren L. et al., 2016, A&A, 595, A4
Luri X., Arenou F., 1997, in Bonnet R. M., ed., ESA SP-402: Hipparcos - Venice '97. ESA, Noordwijk, p. 449
Lutz T. E., Kelker D. H., 1973, PASP, 85, 573
Martell S. L. et al., 2017, MNRAS, 465, 3203
Matijevič G. et al., 2012, ApJS, 200, 14
Michalik D., Lindegren L., Hobbs D., 2015, A&A, 574, A115
Mints A., Hekker S., 2017, A&A, 604, A108
Pasquini L., Randich S., Zoccali M., Hill V., Charbonnel C., Nordström B., 2004, A&A, 424, 951
Perryman M. A. C. et al., 1997, A&A, 323, L49
Pont F., Eyer L., 2004, MNRAS, 351, 487
Press W. H., Flannery B. P., Teukolsky S. A., 1986, Numerical Recipes. The Art of Scientific Computing. Cambridge Univ. Press, Cambridge
Queiroz A. B. A. et al., 2017, MNRAS, 476, 2556
Reddy B. E., 2010, in Cunha K., Spite M., Barbuy B., eds, Proc. IAU Symp. 265, Chemical Abundances in the Universe: Connecting First Stars to Planets. Kluwer, Dordrecht, p. 289
Rieke G. H., Lebofsky M. J., 1985, ApJ, 288, 618
Roederer I. U., Preston G. W., Thompson I. B., Shectman S. A., Sneden C., Burley G. S., Kelson D. D., 2014, AJ, 147, 136
Romano D., Chiappini C., Matteucci F., Tosi M., 2005, A&A, 430, 491
Santiago B. X. et al., 2016, A&A, 585, A42
Schlaufman K. C., Casey A. R., 2014, ApJ, 797, 13
Schlegel D. J., Finkbeiner D. P., Davis M., 1998, ApJ, 500, 525
Schneider F. R. N., Castro N., Fossati L., Langer N., de Koter A., 2017, A&A, 598, A60
Schönrich R., Aumer M., 2017, MNRAS, 472, 3979
Schönrich R., Bergemann M., 2014, MNRAS, 443, 698
Scott D. W., 1992, Multivariate Density Estimation. Theory, Practice, and Visualization. Wiley, New York
Serenelli A. M., Bergemann M., Ruchti G., Casagrande L., 2013, MNRAS, 429, 3645
Sharma S., Bland-Hawthorn J., Johnston K. V., Binney J., 2011, ApJ, 730, 3
Skrutskie M. F. et al., 2006, AJ, 131, 1163
Stassun K. G., Torres G., 2016, ApJ, 831, L6
Steinmetz M. et al., 2006, AJ, 132, 1645
Strömberg G., 1927, ApJ, 65, 238
Thorstensen J. R., 2003, AJ, 126, 3017
Valentini M. et al., 2017, A&A, 600, A66
van Leeuwen F., 2007, Astrophysics and Space Science Library, Vol. 350, Hipparcos, the New Reduction of the Raw Data. Springer-Verlag, Berlin
Wang J. et al., 2016, MNRAS, 456, 672
Wilson J. C. et al., 2010, in Ian S. M., Suzanne K. R., Hideki T., eds, Proc. SPIE Conf. Ser. Vol. 7735, Ground-based and Airborne Instrumentation for Astronomy III. SPIE, Bellingham, p. 77351C
Wojno J., Kordopatis G., Steinmetz M., Matijevič G., McMillan P. J., 2016, in Bragaglia A., Arnaboldi M., Rejkuba M., Romano D., eds, Proc. IAU Symp. 317, The General Assembly of Galaxy Haloes: Structure, Origin and Evolution. Kluwer, Dordrecht, p. 367
Wojno J. et al., 2017, MNRAS, 468, 3368
Wojno J. et al., 2018, MNRAS, preprint (arXiv:1804.06379)
Yang X. L., Chen Y. Q., Zhao G., 2015, AJ, 150, 158
Yuan H. B., Liu X. W., Xiang M. S., 2013, MNRAS, 430, 2188
Žerjal M. et al., 2013, ApJ, 776, 127
Žerjal M. et al., 2017, ApJ, 835, 61

This paper has been typeset from a TEX/LATEX file prepared by the author.